

**TEL AVIV UNIVERSITY**

The Iby and Aladar Fleischman Faculty of Engineering  
The Zandman-Slaner School of Graduate Studies

**REFERENCE-BASED DIFFUSION  
MAPS FOR ONE-CLASS  
CLASSIFICATION: APPLICATION  
TO MINE EXPLOSIONS  
IDENTIFICATION**

A thesis submitted towards the degree of  
Master of Science in Electrical Engineering

by

**Itay Niv**

April 2022

**TEL AVIV UNIVERSITY**

The Iby and Aladar Fleischman Faculty of Engineering  
The Zandman-Slaner School of Graduate Studies

**REFERENCE-BASED DIFFUSION  
MAPS FOR ONE-CLASS  
CLASSIFICATION: APPLICATION  
TO MINE EXPLOSIONS  
IDENTIFICATION**

A thesis submitted towards the degree of  
Master of Science in Electrical Engineering

by

**Itay Niv**

This research was carried out in  
The School of Electrical Engineering  
Faculty of Engineering

Under the supervision of Dr. Neta Rabin and Dr. Yuri Bregman

April 2022

# Acknowledgements

Thank you to my mentor and supervisor, Dr. Neta Rabin, for your patience, guidance, and dedicated support that I will never forget. I'm proud of, and grateful for, my time learning from you.

Thank you to my supervisor, Dr. Yuri Bregman, offering advice and encouragement with a perfect blend of insight and humor. I have benefited greatly from your wealth of knowledge and thoughtful feedback.

Special thanks to my family's unconditional and loving support.

# Abstract

Manifold learning is a branch of machine learning that provides powerful tools for the analysis of high-dimensional and complex data. These methods are particularly suited for developing new robust signal processing techniques, which can organize the datasets according to their underlying parameters while preserving the geometry of the physical-space. For this purpose, a modification of Diffusion Maps (DM), which is a manifold learning geometric-based algorithm, was introduced. This modification incorporates anisotropic kernels into the DM framework. An example for a research area that may be faithfully modeled with such tools is the classification of a specific target class, also known as One-Class Classification (OCC). Manifold learning tools may detect samples that belong to the target class, while providing an explainable organization of the target class samples.

In this work, we propose to model an OCC problem with anisotropic DM, which we refer to as REF-DM. To demonstrate the advantages of our method, we developed a novel application to model an ensemble of seismic events, of a specific target class, related by a common signal-space geometry. We perform automatic identification of mine explosions that originate from a specific mine, given a stream of seismic data, with a low computational cost. The mine pattern to identify is complex and challenging, as it contains diverse seismic events and noise. The capabilities of the application are presented on several large datasets labeled by Israel National Data Center experts and compared with deep learning techniques. Furthermore, we incorporate multi-sensor data fusion techniques and out-of-sample extension in an online manner. Our results show that over 99% of new mine blasts were correctly identified. The proposed method may be adapted to other types of pattern recognition applications, such as speech recognition, and computer vision.

# Table of Contents

<b>Acronyms</b>	<b>iv</b>
<b>List of Figures</b>	<b>v</b>
<b>List of Algorithms</b>	<b>viii</b>
<b>List of Tables</b>	<b>ix</b>
<b>1 Introduction</b>	<b>1</b>
1.1 Manifold Learning for Signal Processing . . . . .	1
1.2 One-Class Classification (OCC) . . . . .	3
1.3 Application: Seismic Signal Processing . . . . .	4
1.4 Thesis Contribution . . . . .	7
1.5 Thesis Structure . . . . .	8
<b>2 Problem Formulation</b>	<b>9</b>
<b>3 Background on Manifold Learning</b>	<b>10</b>
3.1 Diffusion Maps (DM) . . . . .	10
3.2 Hierarchical Data Fusion . . . . .	12
3.3 Anisotropic Diffusion . . . . .	14
3.4 Out-of-Sample Extension . . . . .	15

<b>4 Proposed Method</b>	<b>17</b>
4.1 Reference-based Diffusion Maps (REF-DM) . . . . .	17
4.2 Reference-based Out-of-Sample Extension . . . . .	21
<b>5 Background on Seismology</b>	<b>22</b>
5.1 Seismic Waves and Signals . . . . .	22
5.2 Seismic Data Processing and Analysis . . . . .	23
<b>6 Application of REF-DM for Identification of Mine Explosions</b>	<b>25</b>
6.1 Description of the dataset . . . . .	25
6.2 Problem Formulation and Data Arrangement . . . . .	27
6.3 Feature Extraction . . . . .	29
6.4 Clustering of the Reference Set . . . . .	30
6.5 The training phase . . . . .	31
6.6 The test phase . . . . .	33
<b>7 Experimental Results</b>	<b>35</b>
7.1 Stability of the Embedding . . . . .	35
7.2 Intrinsic Organization of the Mine Blasts Set . . . . .	36
7.3 Classification Outcome . . . . .	40
7.3.1 Comparison with deep learning methods . . . . .	44
<b>8 Conclusions And Future Work</b>	<b>46</b>
<b>9 Publication and Code Implementation</b>	<b>48</b>
<b>Bibliography</b>	<b>49</b>

# Acronyms

**ADM** Anisotropic Diffusion Maps

**CTBTO** Comprehensive Nuclear Test Ban Treaty Origination

**DM** Diffusion Maps

**EIL** Eilat

**GII** Geophysical Institute of Israel

**IMS** International Monitoring System

**INDC** Israel National Data Center

**k-NN** k-nearest neighbors

**OCC** One-Class Classification

**OOSE** out-of-sample extension

**Ref-Clouds** Reference-Clouds

**REF-DM** Reference-based Diffusion Maps

# List of Figures

1.1	Figure courtesy of [1]. Mapping between physical-space and signal-space. Overlapping neighborhoods of points in one space map to overlapping neighborhoods of points in the other, which is the basis for reconstructing the global distribution of sources from observed waveforms. . . . .	3
3.1	An example from [2], for an hierarchical two-level embedding model for fusing four sensors. The bottom-level nodes of the hierarchical structure hold the sensors' embedding manifolds, which are generated using DM. For the top-level processing, DM is applied for the second time. The top-level node fuses together the embedding manifolds of the bottom-level nodes to construct a joint embedding. . . . .	13
4.1	Graph-structured data (the nodes are high-dimensional data-points). Left: Symmetric graph (DM), which includes nodes of $\mathcal{X}$ , and weighed edges according to the local similarity between the data points. Right: A-symmetric graph (REF-DM), where all gray nodes of $\mathcal{X}$ are connected to the purple nodes of $\mathcal{R}$ . . . . .	17
4.2	Left: $W_{ext}$ graph that connects between data-points through their similarity to the reference clouds. Right: $W_{ref}$ graph that connects between the reference clouds through their similarity to the whole data. . . . .	19

4.3 An overview of the REF-DM method. (a) An a-symmetric graph holds the training samples data and the reference clouds data. (b) The anisotropic kernel is constructed from the graph. (c) On top, the reference kernel $W_{ref} = A^T A$ (of smaller size), and on bottom, the external kernel $W_{ext} = AA^T$ (of bigger size). (d) The relationship between the reference kernel's eigenvectors, which are the right singular vectors of $A$ , and the external kernel's eigenvectors, which are the left singular vectors of $A$ . . . . .	20
6.1 Seismic events that belong to the reference set $\mathcal{R}^{ZNE}$ in black, and the EIL station in red. . . . .	26
6.2 Illustration of the training and test datasets. Left: Reference set $\mathcal{R}^{ZNE}$ , which includes waveforms of explosions. Middle: additional training subset $\mathcal{S}^{ZNE}$ , which includes detected and labeled seismic arrivals (extracted from a continuous stream). Right: Test set $\mathcal{Y}_2^{ZNE}$ , which includes detected and unlabeled seismic arrivals (extracted from a continuous stream). . . . .	28
7.1 Training output (of channel E) of Diffusion Maps (DM) versus Reference-based Diffusion Maps (REF-DM) applied to datasets configurations A-D (x-axis and y-axis are the REF-DM coordinates $\psi_1^Z(x)$ and $\psi_2^Z(x)$ , respectively). . . . .	35
7.2 The reference set's embedding computed by Algorithm 2 is presented in all three sub-figures (the x-axis and y-axis are the REF-DM coordinates $\psi_4^Z(x)$ and $\psi_2^Z(x)$ , respectively). Left: The embedding points of the reference set are displayed here as the green cluster of the class of interest, as similarly illustrated earlier in Figure 7.1. Middle: the same points but colored by the LAT value of each event. Right: three example point-clouds that were computed in the reference clustering procedure (Algorithm 1). . . . .	37

7.3 An example of the two characteristics of each of the three colored Ref-Clouds showed in Figure 7.2. The columns are arranged in the order of the clouds: blue, yellow, and red. In the first row, the normalized sonograms (of channel Z) of the center of mass of each point-cloud are shown. In the second row, the first PCA of the covariance matrix characterizes each point-cloud is presented. The markings B1-2, Y1-2, R1-2 denote the features that most characterize each point-cloud and are shared by all sonograms in it (according to the connection between each pair of markings in each column). . . . .	39
7.4 Results of Algorithm 2. The columns are arranged according to the channels as follows: Z, N, E and their fusion, from left to right. The rows are arranged according to the datasets configurations: A, B, C, D, from top to bottom. . . . .	40
7.5 Results of Algorithm 3 plotted by the first two REF-DM coordinates of the training and test sets. The black and blue points belong to the events with the negative label from the training set and test set, respectively. The green points belong to the events from the reference set. The red and pink points belong to the events with the positive label from the training set and test set, respectively. . . . .	42
7.6 Classification Accuracy as function of number of training stream days, where 6 different representation were used. The bold lines belong to the fused diffusion coordinates. . . . .	44

# List of Algorithms

1	Construction of the Reference-Clouds . . . . .	30
2	Reference-based Diffusion Maps (REF-DM) Training phase . . . . .	32
3	Classification of a new detected arrival . . . . .	33

# List of Tables

6.1	Configurations of the datasets . . . . .	29
7.1	Spearman's correlation coefficients and computed p-values between the five available GII seismic catalog's parameters and the first four REF-DM coordinates (dataset configuration C, channel Z). . . . .	38
7.2	Classification results of Algorithm 3 presented by confusion matrices.	43
7.3	The comparison between the fused representations of the classical DM (left column) and REF-DM (right column). . . . .	43

# 1 Introduction

## 1.1 *Manifold Learning for Signal Processing*

Manifold learning is a branch of machine learning that provides powerful tools for the analysis of high-dimensional and complex data. These methods are particularly suited for developing new robust signal processing techniques, which can organize the datasets according to their underlying parameters. The underlying parameters recover and explain the physical phenomena that govern the data. In addition to constructing a compact low-dimensional representation of the data, efficiently, manifold learning approaches embed the data while preserving the geometry of the physical-space and its intrinsic parameters. Due to high dimensionality, ambient noise, and non-linearity in many real-world datasets, these methods are useful for widespread applications, for example, speech recognition, computer vision, recommendation engines, anomaly detection, and bioinformatics.

Diffusion Maps (DM) [3] is a geometric-based algorithm introduced by Coifman and Lafon. Its framework unifies ideas arising in a variety of contexts such as non-linear dimensionality reduction, spectral graph theory, and kernel methods. One of the main benefits of embedding time-series samples into a low-dimensional representation is the ability to define meaningful distances. DM embodies the property that the Euclidean distance between the samples in the embedded-space corresponds to a diffusion distance in the observable signal-space. Diffusion distances measure the similarity between two samples according to their connectivity on the low-dimensional manifold [4].

Signal denoising, image processing, and audio-visual group recognition applications were implemented by diffusion methods [5–7]. Data analysis using DM of fMRI

time-series was introduced in [8–12]. DM was also applied for music analysis and epileptic-seizure prediction [13].

When the nature of the problem is governed by underlying physical phenomena, it is assumed that there are intrinsic parameters that have real physical meaning. DM aims to preserve distances between points in signal-space by mapping them to their counterparts in the embedding. As a result, distortions in the signal-space are reflected as distortions in the embedding. In addition, a challenging issue of DM and its predecessors is that the obtained embedding coordinates may not be unique, because they can be some complicated non-linear functions of the original parameters. We can not guarantee that they describe the underlying drivers of the observable datasets, because the signal is often noisy.

This issue was addressed in [14], and its proposed solution was the use of anisotropic diffusion kernels. By defining a new distance in the signal-space (observable space), the Euclidean distance between points in the inaccessible, physical-space may be approximated. This approach was demonstrated by solving the Non-linear independent component analysis (NLICA) problem. The goal was to better approximate the underlying geometry by associating each data point with a group of nearby points. Then, the pairwise distances take into account the local geometry around each point, this produces cleaner, less distorted diffusion coordinates. In other words, the main idea is to compute the Laplacian on the parameter manifold, whereas classical DM computes the Laplacian on the observable manifold. This method has been also referred to as Anisotropic Diffusion Maps (ADM) [15] and was demonstrated in the analysis of dynamical systems and successful recovery of meaningful coordinates of multiscale chemical reactions. Harris and Dodge also consider that such a geometric model, which is presented in Figure 1.1, is well suited to applications involving underlying physical phenomena, particularly for seismic data analysis. Kushnir et al. [16] integrated ADM with a Nyström-type extension method by using an available set of samples in advance, and using a non-symmetric kernel and extended kernel for unseen samples. It was applied to the classification of electro-magnetic measurements of Earth’s layers structure. Had-dad et al. [17] combined ADM framework with the graph-based filters for extracting textures from images and to identify outliers and anomalies. The same technique was used to suppress transients interference for speech enhancement [18]. In addition, local tangent spaces to the manifold have been explored in [19] by estimating the covariances of the probability densities in time windows using the Mahalanobis distance. Several papers [20, 21] introduce a more sophisticated, adapted approach

for setting the neighborhood size for computing the local information, while taking into account perturbations and noise.

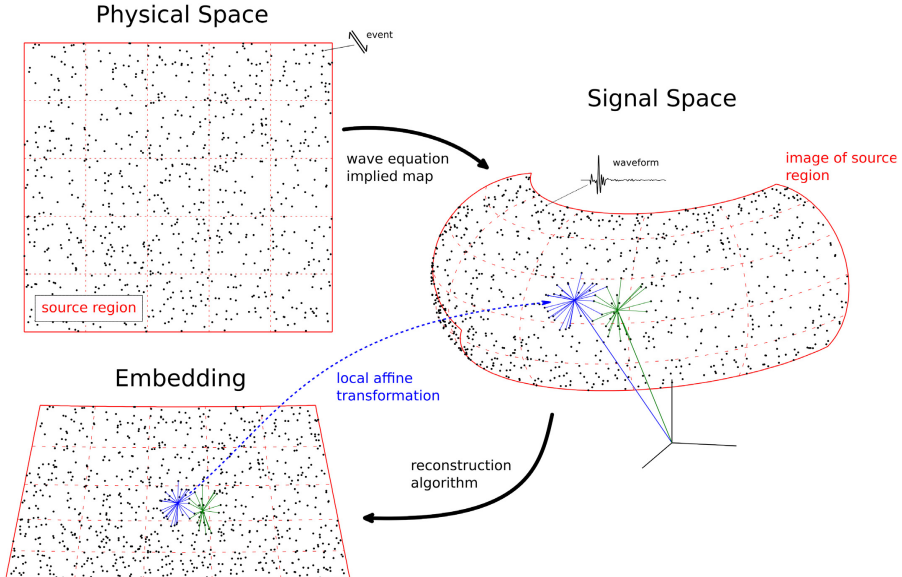


**Figure 1.1:** Figure courtesy of [1]. Mapping between physical-space and signal-space. Overlapping neighborhoods of points in one space map to overlapping neighborhoods of points in the other, which is the basis for reconstructing the global distribution of sources from observed waveforms.

The use of anisotropic diffusion kernels enables to obtain embedding coordinates that are non-linearly invariant, intrinsic parameterization of the empirical data. It has been proven to be a powerful method that enables the development of a whole new field, which clearly still didn't reach its complete potential in terms of modifications and applications. The obtained low-dimensional representation enables to efficiently perform data analysis tasks, such as visualization, clustering, and classification in the reduced space. An example of a research area that may be faithfully modeled with the combination of DM with anisotropic kernels is the classification of a specific target class.

## 1.2 One-Class Classification (OCC)

Identification of data samples of a specific target class (the class of interest) amongst all possible objects, can be considered as One-Class Classification (OCC) problem [22,23]. Many applications of OCC can be found in scientific literature, for

example, outlier detection, anomaly detection, novelty detection, medical imaging, and mobile active authentication. There are several known approaches for modeling OCC tasks, such as Gaussian Mixture Models (GMMs) [24, 25], conditional density estimation of the one-class distribution using Gaussian priors [26], Support Vector Data Description (SVDD) [27], a single layer neural network based on Extreme Learning Machine [28]. A null space-based approach based on kernel Fisher discriminant was proposed in [29] specifically targeting one-class novelty detection. Recently, more innovative methods have been proposed for OCC, for example, CNN to extract attributes from face images of a mobile camera to determine the identity of the user [30]. Various deep feature-based Active Authentication methods have also been proposed for performance comparison [31]. These include autoencoders [32–35], sparse representations for remote sensing [36], self-supervision [37, 38], one class CNN or active authentication and face presentation attack detection [39, 40], Uninformed Students based One-Class Learning (US-OCL) [41], and Progressive knowledge distillation (P-KDGAN) [42]. A known drawback of such algorithms is their *black box* nature, which makes it hard to interpret the underlying features that drive the data analysis results. On the other hand, manifold learning tools enable more explainability of results without a priori knowledge of the model.

### 1.3 Application: Seismic Signal Processing

In this work, we propose to model an OCC problem with anisotropic DM, which is referred to as REF-DM. A compact low dimensional representation of the data is constructed, in which the class of interest patterns is separable from the other data. The combination with anisotropic diffusion kernels enables us to parameterize the empirical data by its intrinsic and meaningful parameters. To demonstrate the advantages of the proposed method, a novel application is developed for modeling an ensemble of seismic events, of a specific target class, related by a common signal-space geometry. An automatic identification of mine explosions that originate from a specific mine is performed, given a stream of seismic data. The variability inside the class of interest is captured by locally preserving its small-scale geometric structures. It is robust to the selection of different training sets. Additionally, manifold-based data fusion techniques are implemented for processing the 3-channel seismic recordings. Furthermore, reference-based out-of-sample extension (OOSE) of newly acquired samples is calculated in an online manner

and with a low computational cost. The mine pattern to identify is complex and challenging, as it contains diverse seismic events and noise.

The application belongs to the field of seismology, the study of earthquakes and seismic waves that move through and around the Earth. Seismology phenomena are often studied by using data-driven models, which are based on various types of data that are monitored and sensed using sophisticated equipment. The large amounts of gathered data make it very attractive for incorporating machine learning techniques. When seismic waveforms have a common, or nearly common, source mechanism, they correspond to an ensemble of events related by common signal-space geometry. Since seismology is driven by underlying physical phenomena, utilization of manifold learning techniques enables to model the data with respect to its intrinsic parameters. While the parameter-space of the data is inaccessible to analyze, the observed signal-space is available. Thus, we expect a geometric-based approach, which parameterizes the data by unique parameters that have real physical meaning, to be best suited for identifying the underlying patterns of the seismic source mechanism. This type of modeling may improve our understanding of the physical phenomena [43].

Automatic identification of mine blasts that originate from a specific mine, from a recording that contains a stream of seismic data, can also be considered as an OCC task. Such an automatic tool would significantly reduce the analyst's workload at many seismological organizations because, in many regions of the world, mine activity accounts for the bulk of the total seismicity. The mine patterns to identify are complex, as the mines span several kilometers and the recorded blasts may be of a different type, magnitude, and location. Identification of such single blasts from ongoing recordings that contain many other types of events, like earthquakes and blasts from other mines, may be a challenging task. Moreover, the arrivals generated by small industrial blasts are nuisance signals for global nuclear explosion monitoring systems (like the one operated by the Comprehensive Nuclear Test Ban Treaty Origination (CTBTO) [44]), because they increase the probability that automatic systems will build false events. As a result, it will be beneficial if small mine explosions were already masked-out at the single-station automatic processing level.

Over the last three decades, different approaches were proposed for the automatic identification of mine blasts. Template-based algorithms are one approach to this problem. It is based on the observation that seismic events with close hypocen-

ters and with similar source mechanisms often generate very similar seismograms while displaying different amplitudes [45]. This enables the creation of templates using the seismograms of strong mine blasts with a high signal-to-noise ratio and subsequently to utilize those templates to detect the weak explosions with a low signal-to-noise ratio. For example, in [46] the author suggested a generalization of the waveform correlation coefficient to compare a single event against a collection of events defining a region. In [47], the selected templates of full seismograms were transformed into sonograms images for better identification. Single-station cross-correlation and clustering using vertical-component traces for an area of high daytime seismicity in eastern Kazakhstan were performed by [48]. In [49], cross-correlation methods have been used for detection, relative location, and magnitude estimation of signals measured by seismic stations in Israel. Those signals belong to a long series of repeated blasts at the Eshidiya phosphate mine in Jordan, and they are used in this work as well. Recently, a dynamic correlation processor [50] was applied to identify the detections of small, repeating local events (e.g., mines) at certain seismic arrays of the International Monitoring System (IMS) to screen them out before the CTBTO global association process [51]. A different approach that relies on recurrent and convolutional neural network models was described in [52], which achieves above 99% classification accuracy between mining blasts and tectonic events in Utah. However, the majority of techniques for OCC have the black box problem. This is a crucial concern for an organization like the CTBTO, which might accuse a country of violating the Geneva convention based on the detection of exceptional seismic events. As a result, the detection algorithms must be interpretable. These predictive models can be such complicated functions of the variables that no human can understand how the variables are jointly related to each other to reach a final prediction. In addition, it is preferable to put away the unnecessary classical template selection procedure, by finding an alternative solution and saving computational costs.

Several DM-based applications, for seismic events classification and other related tasks [53, 54], have been successfully implemented in the last decade. These include earthquake-explosion discrimination using DM [55–58] and aftershock identification [59]. A similar geometric-based approach was recently proposed in [1]. Nevertheless, in the field of seismology, a DM-based application has not yet been implemented for the problem of identification of mine explosions. Furthermore, the use of anisotropic diffusion kernels for this problem is innovative due to its ability to obtain embedded coordinates, which parameterize the empirical data by

unique parameters.

The proposed framework begins with a pre-processing stage, in which a time-frequency representation is extracted from each seismic event. The training phase includes the construction of a low-dimensional representation that separates the class of interest (mine blasts) and the rest of the dataset. The test phase includes an efficient extension of REF-DM for newly arrived samples and ends with a k-nearest neighbors (k-NN) based classification step. In the next section, we will elaborate on the advantages of the proposed method and the contribution of the thesis.

#### **1.4 Thesis Contribution**

The methods developed in this thesis propose a general geometric-based approach for one-class classification. In addition, it provides new tools for seismic signal processing, these exhibit several advantages.

- The method captures the variability within the class of interest as well as preserves the geometric structures of its sub-clustered clouds.
  - It allows better visualization, monitoring, and understanding of the inspected phenomena.
  - There is no need for a traditional template-selection procedure because the whole set of reference samples is used via data-driven modeling.
- The embedding is constructed in a non-symmetric manner, which measures pairwise distances relatively to the class of interest. Thus, it is less sensitive to the selection of different training sets.
- It utilizes manifold-based data fusion techniques for processing the 3-channel seismic recordings, therefore improving the classification.
- The method reveals a low-dimensional coordinate system based on the reference data, and then, in an online manner and at a low computational cost, the coordinate system is extended to newly arriving samples.

We demonstrate the proposed algorithm on several different datasets and highlight its computational and explainability properties. Our results show that over 99% of

new mine blasts were correctly identified. Therefore, incorporating such algorithms in operational stations may dramatically reduce the analysts' burden. Moreover, the explainable nature of manifold learning techniques makes them attractive for such geophysical tasks or other types of pattern recognition applications, such as speech recognition, computer vision, and bioinformatics. Furthermore, the method is capable of providing a visualization, that enhances our understanding of the studied dataset by learning its organization.

We compare our results with several deep learning algorithms, by utilizing transfer learning (i.e. using pre-trained image-based networks). Several known networks are used for this comparison: Visual Geometry Group (VGG) net [60], EfficientNet [61], ResNet [62], and Inception [63]. These were previously used in the context of seismic signal processing [64–66].

## 1.5 Thesis Structure

This thesis is organized as follows. The problem formulation is presented in Chapter 2. The mathematical background and the relevant manifold learning methods are described in Chapter 3. In Chapter 4 the proposed method is presented, REF-DM, as well as the Reference-based OOSE. In Chapter 5, a brief background on seismic signals, data processing, and analysis is provided. In Chapter 6, we demonstrate the application of the proposed method for the identification of mine explosions. Experimental results are presented and discussed in Chapter 7. Finally, conclusions and future research are discussed in Chapter 8.

## 2 Problem Formulation

Let  $\mathcal{R}$  be a historical dataset that holds high-dimensional measurements belonging to a *class of interest*, denoted as the reference set. Let  $\mathcal{S}$  be the additional training subset. It includes detected and labeled measurements. Typically  $\mathcal{S}$  mostly consists of measurements that do not belong to the reference class. Let  $\mathcal{X} = \mathcal{R} \cup \mathcal{S}$  be the combination of the reference set and the additional training subset. Denote  $\mathcal{X}$  as the training set. Let  $\mathcal{Y}$  be the test set. The goal of this work is to train a model based on  $\mathcal{X}$ , and to identify all of the measurements from the test set  $\mathcal{Y}$  that belong to the *class of interest*.

# 3 Background on Manifold Learning

This chapter provides mathematical background and describes the dimensionality reduction techniques that are utilized in this thesis. These are diffusion maps, hierarchical data fusion, anisotropic diffusion, and out-of-sample extension techniques.

## 3.1 Diffusion Maps (DM)

Diffusion maps [3] is a non-linear dimensionality reduction technique, which has been applied to a wide range of signal processing applications [67–70]. The key ingredient in DM is a kernel, which captures the local similarities between the data points. Spectral decomposition of the normalized kernel enables to embed the data into Euclidean space while preserving its geometric structure. Let  $X = \{x_1, \dots, x_N\}$  be a set of data points, the dimension of each point may be high,  $x_i \in \mathbb{R}^D$ . We study the geometric structure of  $X$  by learning local similarities between pairs of data points. In particular, a matrix  $W = w(x_i, x_j)$ , of size  $N \times N$  is computed. Each entry of the matrix holds the weight of the edge that connects  $x_i$  to  $x_j$ . The kernel function  $W = w(x_i, x_j)$  needs to obtain the following properties:

- Symmetric:  $w(x_i, x_j) = w(x_j, x_i)$
- Positive preserving:  $w(x_i, x_j) \geq 0$  for  $x \in X$ .
- Positive semi-definite: for all real valued bounded functions  $f$  defined on  $X$ , it holds that  $\sum_i \sum_j w(x_i, x_j) f(x_i) f(x_j) \geq 0$ .

A Gaussian kernel, which is defined by  $W = w(x_i, x_j) = e^{-\frac{d_c^2(x_i, x_j)}{2\epsilon}}$  obtains the above properties and is a common choice for  $W$ . Here, the cosine distance  $d_c(x_i, x_j) =$

$1 - \frac{\langle x_i, x_j \rangle}{\|x_i\| \cdot \|x_j\|}$ , which computes one minus the normalized dot product of samples  $x_i$  and  $x_j$  is used. The kernel's bandwidth  $\epsilon$  controls the number of points taken into consideration by the kernel. Here, the max–min measure, which was proposed in [71] and was recently applied in [59] and [56] is used for setting  $\epsilon$ . It is computed by  $\epsilon_{MaxMin} = \max_j \min_{i,i \neq j} (d_c^2(x_i, x_j))$ .

To avoid the effect of the non-uniform sampling, the Laplace–Beltrami normalization (see [3]) is applied to  $W$ . This normalization controls the density distribution and is defined by

$$\bar{P} = QWQ, \quad Q_{ii} = \left( \sum_{j=1}^n W_{ij} \right)^{-1}. \quad (3.1)$$

Then, the weighted graph Laplacian normalization is applied to  $\bar{P}$  by

$$P = \bar{Q}\bar{P}, \quad \bar{Q}_{ii} = \left( \sum_{j=1}^n \bar{P}_{ij} \right)^{-1}. \quad (3.2)$$

Both  $Q$  and  $\bar{Q}$  from Eqs. (3.1), (3.2) are diagonal normalization matrices. The spectral decomposition of  $P$  results in two sets of biorthonormal eigenvectors  $\{u_l\}_{l=0}^{N-1}$  and  $\{v_l\}_{l=0}^{N-1}$ . Thus, the elements in  $P$  can be expressed by

$$p(x_i, x_j) = \sum_{l=0}^{N-1} \lambda_l v_l(x_i) u_l(x_j). \quad (3.3)$$

The decaying spectrum allows approximating the sum in Eq. (3.3) by considering only a small number of terms. Therefore, the dimension may be reduced. Finally, the DM embedding coordinates are defined by

$$V(x_i) = (\lambda_1 v_1(x_i), \lambda_2 v_2(x_i), \lambda_3 v_3(x_i), \dots). \quad (3.4)$$

The first eigenvector,  $v_0$ , which is associated with  $\lambda_0 = 1$ , is not included in this definition, as it is constant.

The associated metric named diffusion distance employs the transition matrix  $P$  and its spectral decomposition to define the pairwise preserving distance metric. The diffusion distance is defined as

$$D(x_i, x_j)^2 = \sum_{x_m \in \mathbb{X}} \frac{(p(x_i, x_m) - p(x_m, x_j))^2}{u_0(x_m)}, \quad (3.5)$$

where the denominator holds each point's density. When two points  $x_i$  and  $x_j$  are connected by a large number of paths, the diffusion distance becomes small, meaning that the points are similar. Substituting Eq.(3.3) into the nominator of Eq. (3.5) yields

$$D(x_i, x_j)^2 = \sum_{l=1}^{N-1} \lambda_l^2 (v_l(x_i) - v_l(x_j))^2, \quad (3.6)$$

meaning that the diffusion distance, which is described by the eigenvectors and eigenvalues of the Markov matrix, preserves the geometry of the high-dimensional dataset. The diffusion distance between the data points as defined in Eq. (3.6) corresponds to the Euclidean distance between two points in the low dimensional space.

### 3.2 Hierachial Data Fusion

In real-world applications and processes, there are frequently a lot of sensors that generate parameters (features), and each sensor gathers partial information about the running process. In [2], an unsupervised algorithm for hierachial data fusion was suggested and demonstrated for anomaly detection in multi-dimensional time series, using diffusion approach. These input sensors were fused to describe the overall process behavior. The suggested data fusing algorithm was done in a hierarchical manner, beginning with pre-processing the input sensors. A two-level embedding fusion model is applied in this work, as depicted in Figure 3.1. Yet, the hierarchical model can be generalized for additional levels, as detailed in [2].

We assume a multidimensional sensor array of  $S$  sensors gathers data on a dynamic process. Each sensor's data is pre-processed. To produce a hierarchical tree-shaped structure that holds embedding manifolds, the dataset is processed in a bottom-up fashion. The leaf nodes will be referred to as bottom-level nodes, the tree root will be referred to as a top-level node. The bottom-level nodes of the hierarchical structure hold  $S$  embedding manifolds, which are generated using DM. Each sensor is handled independently at the bottom level. The DM unfolds the geometric structure of each sensor's pre-processed data. The diffusion coordinates of sensor  $s \in S$  are defined by  $V_s = (\lambda_1 v_1, \lambda_2 v_2, \dots, \lambda_d v_d)$ . Since the diffusion kernel measures distances within a single sensor, the original inputs sensors can be of different scales. This process bypasses the need to scale the sensors (parameters, features) if heterogeneous datasets are processed.

For the top-level processing, DM is applied for the second time, to the concatenation of the diffusion coordinates  $V = (V_1 V_2 \dots V_S)$ . The top-level node in the hierarchy fuses together the embedding manifolds of the bottom-level nodes to construct a joint embedding that gives a full description of the dynamic process. The hierarchical embedding tree provides a flexible structure, which can be adapted to the input data.

### Hierarchical two level embedding

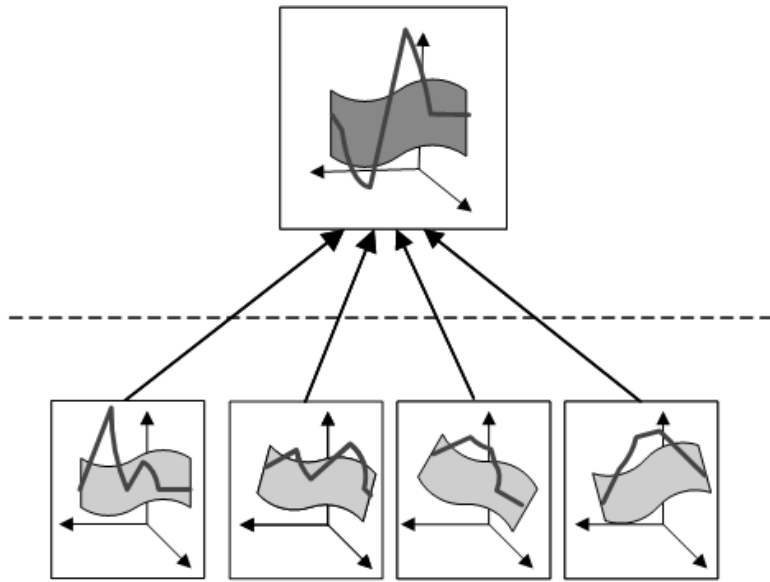


**Figure 3.1:** An example from [2], for an hierarchical two-level embedding model for fusing four sensors. The bottom-level nodes of the hierarchical structure hold the sensors' embedding manifolds, which are generated using DM. For the top-level processing, DM is applied for the second time. The top-level node fuses together the embedding manifolds of the bottom-level nodes to construct a joint embedding.

In this work, we implemented the hierarchical two-level data fusion algorithm for time-frequency input data, which is gathered by three sensors. We will further elaborate on its utilization in Section 6.5 and Algorithm 2.

### 3.3 Anisotropic Diffusion

When the nature of the problem is governed by underlying physical phenomena, it is assumed that there are intrinsic parameters that have real physical meaning. DM aims to preserve distances between points in signal-space by mapping them to their counterparts in the embedding. As a result, distortions in the signal-space are reflected as distortions in the embedding. ADM [14, 15] constructs a new distance in the signal-space (observable space) that approximates the Euclidean distance between points in the parametric-space (inaccessible space).

Let  $x_i \in X$  be the observable characteristics, assumed to be the outcome of a nonlinear, smooth, and bi-Lipschitz transformation  $f : Y \rightarrow X$  of the parametric features  $y_i \in Y$ . Let  $y, \eta \in Y$  be such that  $x = f(y)$  and  $\eta = f(\eta)$ , and assume that the parametric features  $y$  follow an Itô process as stated in [14]. It can be shown then that

$$\|\eta - y\|^2 = \frac{1}{2}(\xi - x^T)[(JJ^T)^{-1}(x) + (JJ^T)^{-1}(\xi)](\xi - x) + \mathcal{O}(\|\xi - x\|^4), \quad (3.7)$$

where  $J$  represents the Jacobian matrix, i.e. the distortion of the transformation  $f$ . Using the Itô process assumption and applying an appropriate rescaling of the features, the unknown Jacobian-based distortion that appears in the new distance can be locally estimated by the covariance matrix of the data, i.e.,  $\Sigma = JJ^T$ . In other words, the distortion can be measured using a *local* Mahalanobis distance to be applied to points nearby to a given one. More precisely, for points  $x_k \in X$ , we define the distance

$$D_{AD}(x_i, x_j) = (x_i - x_j)^T[\Sigma^{-1}(x_i) + \Sigma^{-1}(x_j)](x_i - x_j), \quad (3.8)$$

The covariances  $\Sigma(x_i)$  can be estimated using clouds of points around  $x_i$ . It is sometimes easier to estimate  $D_{AD}$  by using simply the pseudo-inverse of the covariance matrix of only  $x_i$ , rather than both  $x_i$  and  $x_j$ . Once we have  $D_{AD}(x_i, x_j)$  we can define an anisotropic kernel similarity matrix  $W_{i,j} = e^{-\frac{D_{AD}(x_i, x_j)}{\sigma}}$  and apply the same steps of the isotropic procedure that are used to compute the DM projections.

### 3.4 Out-of-Sample Extension

It is critical in many applications to be able to apply the low-dimensional representation generated on a training set to new data samples. The construction of diffusion map coordinates requires the spectral decomposition of a  $N \times N$  matrix, where  $M$  is the number of data points. When  $N$  is large (for example, tens of thousands of data points), this technique is time expensive and should not be used for each new arriving sample. The Nyström technique [72, 73] has traditionally been used to extend nonlinear embedding coordinates. Other multiscale techniques for extension include spectral multi-scale function extensions [74] or Laplacian Pyramids [75].

In this thesis, the geometric harmonics method [76] was applied for the extension of the classical DM. It is based on the Nyström technique. The method involves the construction of harmonic functions that form a basis and thus can span a given function  $f$ . In particular, the harmonic functions are used to span and extend the diffusion maps embedding coordinates.

Let  $X$  be a set of points in  $\mathbb{R}^D$  and  $f(x) = \lambda_1\psi_1(x)$  be the corresponding first diffusion maps embedding map. Let  $\bar{x} \in \mathbb{R}^D$  be a new data point. The geometric harmonics scheme extends  $f(x) = \lambda_1\psi_1(x)$  to  $\bar{x}$ , it evaluates  $f(\bar{x}) = \lambda_1\psi_1(\bar{x})$ .

We form a basis that can span any given function  $f$ . The basis is composed of eigenvectors associated with a kernel matrix. A kernel (typically a Gaussian kernel) with a bandwidth scale equal to  $\sigma > 0$  is constructed from the data set  $X$ . The parameter  $\sigma$  is the scale of the extension, which depends on the smoothness of the approximated function (see [76]). In general, it is desirable that  $\sigma$  would be larger than  $\epsilon$ , which was the kernel width that was set in diffusion maps. Denote this kernel by  $W_\sigma = w_\sigma(x_i, x_j) = e^{-\frac{\|x_i - x_j\|^2}{2\sigma}}$  and compute its spectral decomposition. The eigenvalues and eigenvectors of  $W_\sigma$  are denoted by  $\{\mu_k\}_{k=0}^{M^1}$  and  $\{\psi_k\}_{k=0}^{M^1}$ , they satisfy

$$\mu_k \psi_k(x_i) = \sum_{x_j \in X} e^{-\frac{\|x_i - x_j\|^2}{\sigma}} \psi_k(x_j), x_i \in X. \quad (3.9)$$

Now, a general function  $f$  and in particular  $f(x) = \lambda_1\psi_1(x)$ , can be approximated as a linear combination of this basis by

$$\lambda_1 \psi_1(x_i) = f(x_i) = \sum_{k:\mu_k \geq \eta\mu_0} < \psi_k, f > \psi_k(x_i), x_i \in X. \quad (3.10)$$

Since the eigenvalues  $\{\mu_k\}$  tend to zero as  $k \rightarrow \infty$ , the scheme in Eq. 3.9 is ill-conditioned. In order to avoid this ill-conditioning, the geometric harmonics cuts off the sum in Eq. 3.10 by introducing a parameter  $\eta$  and only using the eigenvectors that satisfy  $\mu_k \geq \eta\mu_0$ . Note that this procedure, which includes the construction of the kernel  $W_\sigma$  and calculation of its eigenvalues and eigenvectors, is only carried out once as a pre-processing step. Evaluating the embedding location of a new point  $\bar{x}$  in an online mode only requires the two following steps (Eq. 3.11 and Eq. 3.12), which are fast to compute. The functions in the basis  $\{\psi_k\}_{k:\mu_k \geq \eta\mu_0}$  are extended to the point  $\bar{x}$  by

$$\bar{\psi}_k(\bar{x}) = \sum_{x_j \in X} e^{-\frac{\|\bar{x}-x_j\|^2}{\sigma}} \psi_k(x_j). \quad (3.11)$$

The diffusion coordinate  $f = \lambda_1 \psi_1$  is extended to the new point  $\bar{x}$  by

$$\lambda_1 \psi_1(\bar{x}) = f(\bar{x}) = \sum_{k:\mu_k \geq \eta\mu_0} < \psi_k, f > \bar{\psi}_k(\bar{x}). \quad (3.12)$$

Extension of the next diffusion maps coordinates  $\lambda_2 \psi_2, \lambda_3 \psi_3, \dots$  is done in a similar manner, with the use of the same basis  $\{\mu_k\}, \{\psi_k\}$ .

# 4 Proposed Method

## 4.1 Reference-based Diffusion Maps (REF-DM)

This section describes a modification of the DM algorithm. It follows ideas from [16] and utilizes the Anisotropic Diffusion Maps (ADM) algorithm as the foundation on which our proposed method, REF-DM is based. ADM acts as an explainable filter for detecting the class of interest as well as preserving its organization and structure.

The low-dimensional representation is constructed, like in DM, by a spectral decomposition of a kernel. However, as displayed in Figure 4.1, the kernel, which captures the pairwise distances between the data points (the gray nodes in the figure), is calculated with respect to the points' distance from a subset of the points that belong to the class of interest (the purple nodes in the figure). We assume that the reference set, which holds points from the class of interest, is denoted by  $\mathcal{R} = \{r_1, \dots, r_{N_R}\}$  and is available in advance.

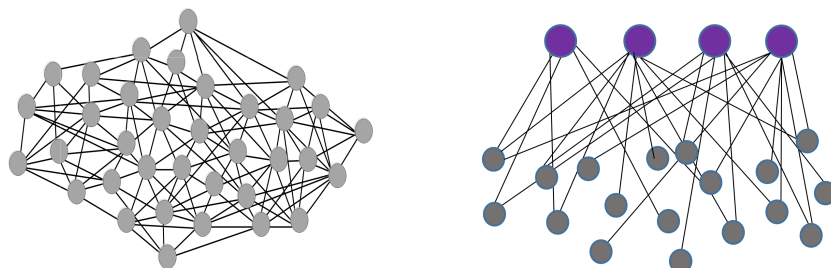


**Figure 4.1:** Graph-structured data (the nodes are high-dimensional data-points). Left: Symmetric graph (DM), which includes nodes of  $\mathcal{X}$ , and weighed edges according to the local similarity between the data points. Right: A-symmetric graph (REF-DM), where all gray nodes of  $\mathcal{X}$  are connected to the purple nodes of  $\mathcal{R}$ .

The subset  $\mathcal{R}$  is clustered into  $K$  groups, each group is denoted by  $\{\mathcal{C}_k\}_{k=1}^K$  and

referred to as a cloud of data points. Ideally, the clustering should be done according to some prior knowledge regarding the similarity between the data points in  $\mathcal{R}$ . For example, if there is a time parameter in the system like in [77], then a cluster may hold data points that are generated consecutively. In [78] a cloud was formed from data points that belong to the same spatial body location. The process of defining the clouds in this thesis is addressed in Section 6.4.

As proposed in [17], each point cloud  $\mathcal{C}_k$ , is characterized by its center of mass  $m_k$ , and its covariance matrix  $\Sigma_k$ , which characterizes the tangent space at  $m_k$ . The availability of the reference set allows for the computation of the characteristics of each cloud  $k$  in advance. There is no need for a traditional template-selection procedure in the proposed method because the whole set of reference samples is used via data-driven modeling.

Following [16, 79, 80] an a-symmetric pairwise metric between any new sample  $x \in \mathcal{X}$  and a reference sample  $r \in \mathcal{R}$  is computed. This defines a new distance in the high-dimensional space that captures the organization of the data points according to the underlying physical driving phenomena [14]. It codes the distances between the reference points of the clouds  $\mathcal{C}_k$  and each other data point in the set. The Mahalanobis distance is utilized, in particular, the mean  $m_k$  and covariance  $\Sigma_k$  of the point cloud are computed. In a slight abuse of notations, we next refer to the distance between a point  $x$  and a cloud  $C_k$  as the distance between  $x$  and  $k$ .

The corresponding affinity matrix of size  $N \times K$  is defined by  $A = a(x, k) = \exp\left\{-\frac{d(x, k)}{\epsilon}\right\}$  and constructed by

$$A = a(x, k) = \exp\left\{-\frac{(x - m_k)^T \Sigma_k^\dagger (x - m_k)}{\epsilon}\right\}, \quad (4.1)$$

where  $\epsilon > 0$  is a tunable kernel scale. The construction of  $A$  requires the calculation of the pseudo-inverse of the covariance matrices that are associated with  $C_k$ , hence, there is no need to compute the covariance matrix of the whole training set  $\mathcal{X}$ . The similarity weights defined in Eq. (4.1) are organized into a similarity matrix  $A = (a(x, k))_{x \in \mathcal{X}, k \in 1, \dots, K}$ , where  $k$  is the cloud's index.

We now look at the set of training samples  $\mathcal{X}$  as a graph (i.e. each node represents a sample). The similarity between any two samples  $x_i$  and  $x_j$  is calculated relatively

to the reference set by

$$w_{ext}(x_i, x_j) = \sum_{k=1}^K a(x_i, k)a(x_j, k). \quad (4.2)$$

The similarity is strong if these samples are close to many common neighbors in the reference set  $\mathcal{R}$ . Then, the dual extended kernel between the new samples, which is of size  $N \times N$ , is defined by  $W_{ext} = AA^T = (w_{ext}(x_i, x_j))_{x_i, x_j \in \mathcal{X}}$ . The latter can be interpreted as an affinity measure between any pair of new samples  $x_i$  and  $x_j$  via all the clouds. The associated reference kernel, which defines the similarity between pairs of reference clouds  $k$  and  $k'$  through the entire dataset, is defined by

$$W_{ref} = A^T A = (w_{ref}(k, k')). \quad (4.3)$$

Illustration of the two kernels  $W_{ext}$  and  $W_{ref}$  is shown in Figure 4.2. By comparing the sizes of  $W_{ref}$  and  $W_{ext}$ , notice that  $W_{ref}$  (of size  $K \times K$ ) is much smaller than  $W_{ext}$  (of size  $N \times N$ ). Thus, computing the eigenvectors of  $W_{ref}$  instead of  $W_{ext}$  is computationally efficient and reduces the complexity of the problem. It should be noted, that the two sets of eigenvectors are related, as we further review.

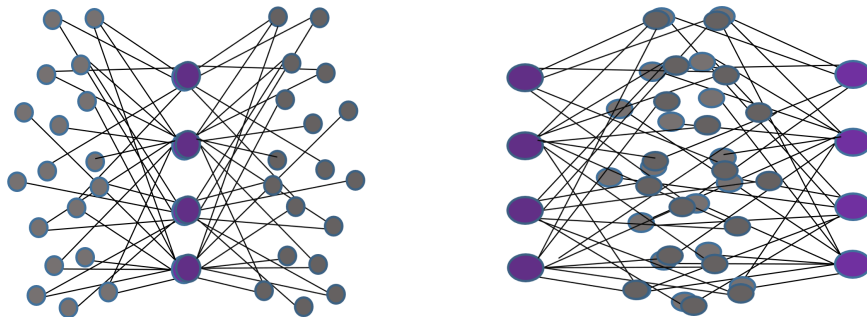


**Figure 4.2:** Left:  $W_{ext}$  graph that connects between data-points through their similarity to the reference clouds. Right:  $W_{ref}$  graph that connects between the reference clouds through their similarity to the whole data.

Since we are interested in the Laplace–Beltrami normalization, the kernel  $A$  is modified. First, the diagonal density matrix, denoted by  $D_1$ , whose diagonal elements are the sum of rows of  $W_{ref}$ , and given by

$$d_1(k) = \sum_{k' \in K} w_{ref}(k, k') \quad (4.4)$$

is computed. Then, another diagonal matrix  $D$  is defined, whose diagonal elements are the sum of rows of  $AD_1^{-1}$ . It is given by

$$d(x) = \sum_{k=1}^K \frac{a(x, k)}{d_1(k)}. \quad (4.5)$$

Last, the non-symmetric anisotropic kernel is constructed by

$$\bar{A} = D^{-1}AD_1^{-1} = \left( \frac{a(x, k)}{d(x)d_1(k)} \right). \quad (4.6)$$

The matrices  $\bar{W}_{ext} = \bar{A}\bar{A}^T$  and  $\bar{W}_{ref} = \bar{A}^T\bar{A}$  share the same eigenvalues  $\{\lambda_l\}$ , which are non-negative, bounded by 1 and sorted in decreasing order with  $\lambda_1 = 1$ . The corresponding first eigenvector is the trivial column-vector of ones.

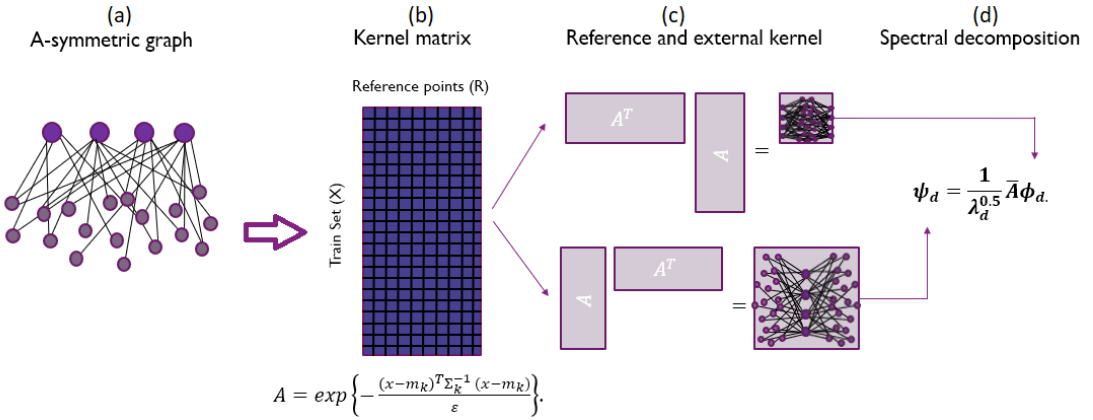


**Figure 4.3: An overview of the REF-DM method.** (a) An a-symmetric graph holds the training samples data and the reference clouds data. (b) The anisotropic kernel is constructed from the graph. (c) On top, the reference kernel  $W_{ref} = A^T A$  (of smaller size), and on bottom, the external kernel  $W_{ext} = A A^T$  (of bigger size). (d) The relationship between the reference kernel's eigenvectors, which are the right singular vectors of  $A$ , and the external kernel's eigenvectors, which are the left singular vectors of  $A$ .

Notice that the eigenvectors  $\{\phi_l\}$  of  $\bar{W}_{ref}$  are the right singular vectors of  $\bar{A}$ , and the eigenvectors  $\{\psi_l\}$  of  $\bar{W}_{ext}$  are the left singular vectors of  $\bar{A}$ . As discussed in [4], the right singular eigenvectors represent the underlying structure of the clouds, and the left singular eigenvectors naturally extend this representation to the new

samples [16, 17]. The relationship between the two sets is given by

$$\psi_l = \frac{1}{\lambda_l^{1/2}} \bar{A} \phi_l. \quad (4.7)$$

The normalization term  $\lambda_l^{1/2}$  ensures that  $\|\psi_l\|_2 = \|\phi_l\|_2$ . Furthermore, Eq. (4.7) maps the orthonormal family  $\{\phi_l\}_{l=1}^{K-1}$  onto the orthonormal family  $\{\psi_l\}_{l=1}^{K-1}$ . As visualized in Figure 4.3, this relationship connects between the geometry of the reference set to the geometry of the external set.

The orthogonality gives us a trivial way to project onto any vector space spanned by given eigenfunctions. In practice, only the leading eigenvalues (and corresponding eigenvectors) in Eq. (4.7) satisfying  $\lambda_l \geq \delta \lambda_0$  are kept. Denote the space spanned by the first  $l^*$  eigenvectors as  $\Psi = \{\psi_l\}_{l=1}^{l^*}$ . Out-of-sample extension of the embedding coordinated to new data points is discussed in the next section.

## 4.2 Reference-based Out-of-Sample Extension

Let  $y$  be a test sample from the high-dimensional space,  $y \in \mathcal{Y}$ . The goal is to extend the coordinates  $\Psi$  to  $y$ , i.e. to evaluate  $\Psi(y)$ . The test sample  $y$  is processed similarly to the training samples. First, a row-vector  $A' = (a'(y, k))_{k \in 1, \dots, K}$ , that holds the distances between  $y$  and the point clouds from the training phase is constructed based on Eq. (4.1). Then,  $d(y)$  is computed from Eq. (4.5) by dividing each element  $a(y, k)$  by  $d_1(k)$  ( $d_1(k)$  is computed from the training set). Next,  $A'$  is normalized as described in Eq. (4.6) by using  $d(y)$  instead of  $d(x)$  to generate  $\bar{A}'$ . Finally, Eq. (4.7) is evoked with  $\bar{A}'$  and the eigenpairs  $\{\phi_l, \lambda_l\}_{l=1}^{l^*}$  that are calculated in the training phase. This extends the embedding  $\Psi' = \{\psi'_l\}_{l=1}^{l^*}$  to include the test point.

# 5 Background on Seismology

Seismology is the study of earthquakes and seismic waves that move through and around the Earth. The field also includes studies of earthquake environmental effects such as tsunamis as well as diverse seismic sources like volcanic, tectonic, oceanic, atmospheric, and man-made explosion processes. One of the key problems in seismology is to solve the inverse problem, i.e., to derive from the analysis of seismic records information about the structure and physical properties of the Earth medium. Seismology is driven by observations, thus, improvements in instrumentation and data availability had always contributed to the progress in seismology theory and in our understanding of Earth's structure.

This chapter includes two parts. The first part explains seismic waves and signals, and the second part describes seismic data processing and analysis.

## 5.1 Seismic Waves and Signals

There are several different kinds of seismic waves, and they all move in different ways and with different velocities [81]. The two main types of waves are body waves and surface waves. A body wave is a seismic wave that moves through the interior of the Earth, as opposed to surface waves that travel near the Earth's surface. There are two types of body waves, pressure waves or primary waves (P-waves) and shear or secondary waves (S-waves).

Seismic waves are recorded by seismometers that measure the motion of the ground. Most modern seismometers include three separate channels that allow the determination of the simultaneous movement in three different directions: up-down (Z), north-south (N), and east-west (E). We denote by ZNE, datasets that consist of three-component measurements. A typical seismic station consists of a three-component (3-channel) seismometer, a GPS clock for determining time, and

a recorder for collecting data [82]. A recording of Earth’s motion measured at the location of the sensor as a function of time is called a seismogram (a seismic waveform). S-waves are slower than P-waves. Therefore, in the seismograms, the recording of S-waves (S-phase) appears later than P-phase. Some of the seismic stations were equipped with seismic arrays, which improve the signal-to-noise ratio (SNR) by finding directional information [83].

## 5.2 Seismic Data Processing and Analysis

Seismic data processing includes seismic signal detection and phase picking, calculation of the origin time and location of the hypocenter (i.e. rupture starting point) and seismic event characterization (estimation of magnitudes and event classification) [84]. The signal detection and the phase picking are performed using the waveforms of each station separately, while the event location and characterization are network-level processing tasks, which involve multiple station processing. A significant step of event location is seismic phase association, i.e. the task of linking together phase detections on different seismometers that originate from a common seismic source. The analysis results are compiled in a seismic bulletin, i.e. a catalog including the hypocenter parameters together with the attributes of all detected phases (i.e. station, phase arrival time, amplitude, etc).

An important development in automatic seismic detection was the STA/LTA trigger-based algorithm [85–87], introduced in the late 1970s. It utilizes as a criterion for picking the ratio of continuously calculated average energy (or envelope or absolute amplitude) of a recorded trace in two consecutive moving-time windows of different lengths. The first calculates a short time average (STA), which captures the signal energy, and the second calculates a long-term average (LTA) estimates the current energy of the noise.

A large number of machine learning papers that present applications to seismic event identification and classification rely on computing a time-frequency representation of the signal as a first phase, and processing it to extract features as a second step. The processed time-frequency representations are then fed as input to a machine learning algorithm.

Today, the analysis tasks in most seismic observatories start with near real-time automatic processing that implements automatic signal detection and P-phase picking, hypocenter’s localization, and magnitude determination. However, the current

quality of most automatic seismic bulletins is insufficient. For instance, around half of the events included in the global automatic bulletin, named Standard Event List, that is produced by the CTBTO in Vienna are later not approved by the human analyst [88]. Therefore, seismological institutes rely heavily on manual analysis for performing routine tasks. Seismologists interactively revise and correct the automatic bulletins based on scientific reasoning, their knowledge, and practical experience.

# 6 Application of REF-DM for Identification of Mine Explosions

This chapter presents the application of the REF-DM methods for the identification of mine explosions that originated in the Eshidiya mine area in Jordan. We begin by describing the dataset in Section 6.1. In Section 6.2 the problem of mine explosion identification and the data arrangement are defined. The feature extraction procedure is depicted in Section 6.3. Then, the clustering procedure of the mine blasts reference set is detailed in Section 6.4, followed by a description of the training and test stages of the classification algorithm in Section 6.5 and Section 6.6

## 6.1 Description of the dataset

Our goal is to identify the arrivals caused by the explosions at the Eshidiya mine in Jordan out of continuous waveforms from the Eilat (EIL) station. Eshidiya phosphate mine is located in southern Jordan in an area that spans approximately  $300 \text{ km}^2$ . Production at the Eshidiya mine started in 1988 and its annual production capacity is about 5 million tons [89, 90]. The production is accomplished with intensive blasting which is carried out with different yields, at two main sites, and at different depths. The distance between the epicenters can be 20 km or more, which causes a lot of variability in the seismic recordings of explosions.

The 3-component broadband seismic station EIL in Israel is located at a distance of 125 km from the Eshidiya mine. EIL is the International Monitoring System (IMS) auxiliary seismic station AS48 affiliated with the Comprehensive Nuclear Test Ban Treaty Origination (CTBTO) and it is also a part of the Israel National Seismic Network [91]. The station is equipped with a Streckeisen STS-2 seismometer and a Nanometrics Europa digitizer. The sampling frequency is 40 Hz.

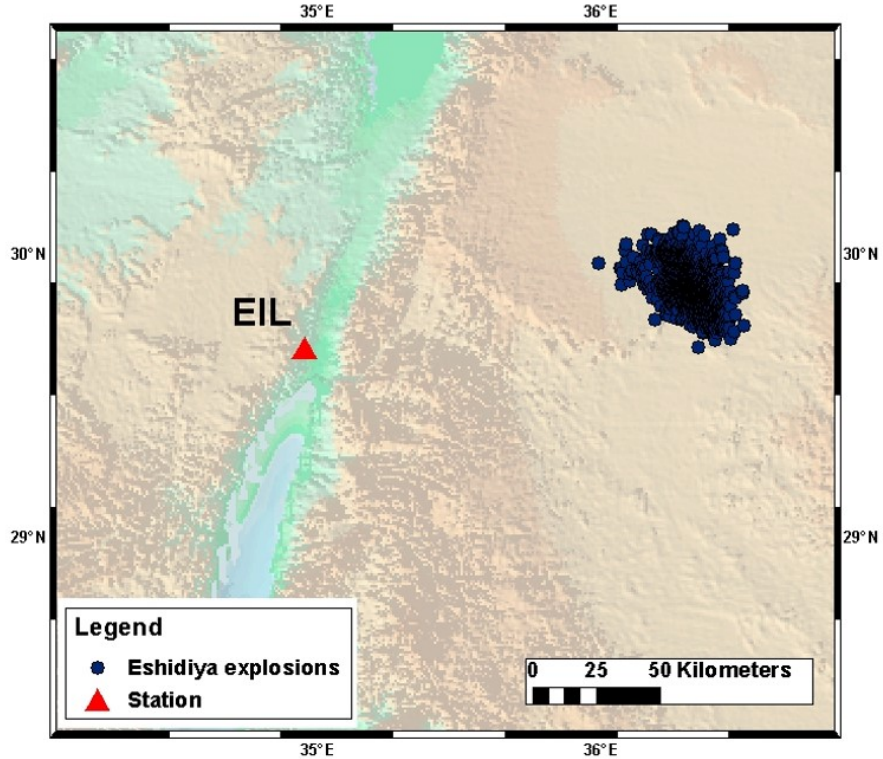


**Figure 6.1: Seismic events that belong to the reference set  $\mathcal{R}^{ZNE}$  in black, and the EIL station in red.**

In this study, the three following datasets recorded at EIL station are used. The first dataset includes 1196 seismograms of explosions at the Eshidiya mine recorded between 2004 and 2015 (see a map of the region in Figure 6.1). This dataset was formed by matching the set of 1562 explosions in the Eshidiya mine area reported by Israel National Data Center (INDC) [49] with the set of 1196 from the seismic catalog of Geophysical Institute of Israel (GII). We included only the 1196 explosions that appear in both datasets. These 1196 events will be later used as the reference set. Note that estimated durational magnitudes existed for only 1038 (87%) out of the 1196 explosions. These magnitudes have values from 0.8 to 2.8 with a median equal to 1.8. Each seismogram in the dataset is a 50-seconds long recording that has been trimmed so that there are 5 seconds before its P phase onset. The reference dataset was used in previous research [49] and [56].

The second and the third datasets contain 1035 and 492 continuous waveforms, respectively, from the EIL station. The second dataset was recorded in March 2011 and the third dataset was recorded on April 11 – 20, 2015. During these periods,

two major seismic events occurred: the Tôhoku earthquake with magnitude 9 on March 11, 2011 and the Crete earthquake with magnitude 5.6 on April 16, 2015, at teleseismic and regional distances from the EIL station, respectively. Besides the waveforms, the datasets include 1035 and 492 automatic arrivals, respectively, detected at the EIL station by the CTBTO. We have labeled the arrivals as positive if they relate to an explosion at the Eshidiya mine according to the GII seismic catalog. Otherwise, the arrivals are labeled negative. As we will show below, the datasets have some minor label errors, as the ground truth information is not available.

## 6.2 Problem Formulation and Data Arrangement

We provide several notions for the training and the test sets and formulate the problem of mine explosion identification.

Let  $\mathcal{R}^{ZNE}$  be a reference set that comprises of sonovectors (these are the features extarcted from each arrival, see Section 6.3) from 1196 historic explosions in the Eshidiya mine area in Jordan. The reference set belongs to a *class of interest*, and it will always be a part of the training set. For each event  $i$ , three sonovectors are computed, one for each channel. Denote the three sonovectors that belong to a single mine event by  $r_i(t) \in \mathcal{R}^{ZNE}$ . Thus,  $\mathcal{R}^{ZNE} = \{\mathcal{R}^Z, \mathcal{R}^N, \mathcal{R}^E\} = \{(r_i^Z(t); r_i^N(t); r_i^E(t))\}_{i=1}^{N_R}$ , where  $N_R = 1196$  is the number of events in the reference set.

In order to include negative examples into the training set, we define  $\mathcal{S}^{ZNE}$  to be an additional training subset of sonovectors, which consists of three channels as well. This subset is determined by arrivals that were extracted from continuous waveforms recorded in March 2011 and April 2015. Analogously to the reference set, each event is a 50-seconds long waveform segment that is cut out of continuous seismogram, while the arrival resides 5 seconds after the beginning of the segment. The arrivals are labeled positive or negative while most of them are negative (i.e. do not belong to the arrivals of Eshidiya mine explosions).

Thus,  $\mathcal{S}^{ZNE} = \{\mathcal{S}^Z, \mathcal{S}^N, \mathcal{S}^E\} = \{(s_i^Z(t); s_i^N(t); s_i^E(t))\}_{i=1}^{N_S}$ , where  $N_S$  is the number of arrivals extracted from the continuous waveforms. Let  $\mathcal{X}^{ZNE} = \mathcal{R}^{ZNE} \cup \mathcal{S}^{ZNE}$  be the combination of the reference set and the additional training subset. Denote  $\mathcal{X}^{ZNE}$  as the training set.

Let  $\mathcal{Y}^{ZNE}$  be the test set of sonovectors that were created like the ones in the

training set. This set holds unlabeled arrivals, which were extracted from a continuous stream. It is denoted by  $\mathcal{Y}^{ZNE} = \{\mathcal{Y}^Z, \mathcal{Y}^N, \mathcal{Y}^E\} = \{(y_i^Z(t); y_i^N(t); y_i^E(t))\}_{i=1}^{N_Y}$ , where  $N_Y$  is the number of events in the test set.

The goal of this work is to train a model with the training set  $\mathcal{X}^{ZNE}$ , and identify all of the events from the test set  $\mathcal{Y}^{ZNE}$  that belong to the *class of interest*. The formulation of the training and test datasets is depicted in Figure ??.

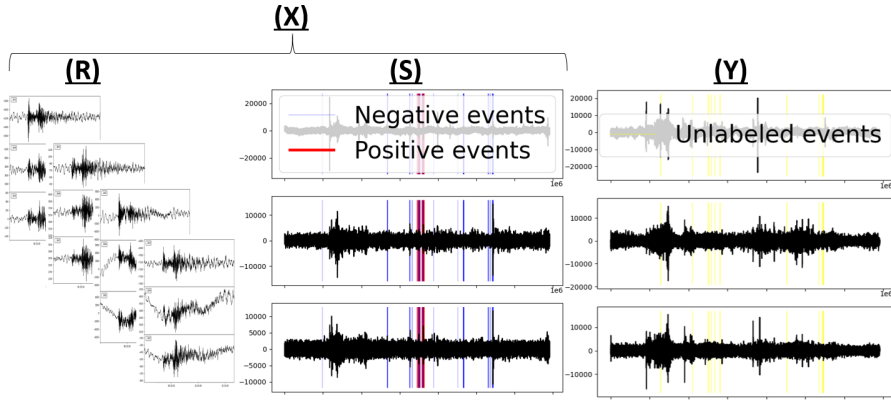


**Figure 6.2: Illustration of the training and test datasets. Left: Reference set  $\mathcal{R}^{ZNE}$ , which includes waveforms of explosions. Middle: additional training subset  $\mathcal{S}^{ZNE}$ , which includes detected and labeled seismic arrivals (extracted from a continuous stream). Right: Test set  $\mathcal{Y}_2^{ZNE}$ , which includes detected and unlabeled seismic arrivals (extracted from a continuous stream).**

Different training sets that use the data recorded in March 2011 and April 2015 are examined. Therefore, the size of the additional training subset  $\mathcal{S}^{ZNE}$  changes in the different experiments that are described below. Table 6.1 contains four rows that correspond to four training subset configurations, named A-D. The table shows the number of arrivals used for the training set of each configuration with reference to the datasets that were described in Section 6.1. Note that the training set sizes increase from top to bottom.

Two additional test sets are defined as follows.

- Test set  $\mathcal{Y}_1^{ZNE}$ : 845 sonograms from March 9-31, 2011 (the remaining part of the second dataset).
- Test set  $\mathcal{Y}_2^{ZNE}$ : 492 sonograms from April 11-20, 2015 (the third dataset).

**Table 6.1: Configurations of the datasets**

Training set		
Ref. set	Additional training subset	
2014-2015	March 2011	April 2015
<b>A</b>	1196	190
<b>B</b>	1196	-
<b>C</b>	1196	1035
<b>D</b>	1196	1035
		492

### 6.3 Feature Extraction

Feature extraction is a preprocessing step that is carried out before dimensionality reduction. A time-frequency representation, named sonograms [92], is used, with some modification. The sonogram is normalized, as explained in [56, 59].

In this work, the length of a raw single-trace seismic signal is 2000 samples. The Short-Time Fourier Transform is applied to the signals with a Hanning-tapered window size of 128 samples and an overlap of 0.8. Then, power spectral densities are computed and yield a spectrogram. The sonogram is obtained by summing the spectrogram in near half-octave logarithmically scaled frequency pass-bands for every time bin. The following seven frequency passbands are used in this study: 0.318 – 0.635 Hz, 0.635 – 1.27 Hz, 1.27 – 2.222 Hz, 2.222 – 3.81 Hz, 3.81 – 6.032 Hz, 6.032 – 9.206 Hz, 9.206 – 13.65 Hz and 13.65 – 20 Hz (see previous work [55]). Then, the sum of the energy in each frequency band is normalized to 1. The resulted normalized sonogram is denoted as  $s(f, t)$  where  $f$  is the frequency band number and  $t$  is the time-window number. Here  $f \in \{0, \dots, 6\}$  and  $t \in \{0, \dots, 74\}$ . Finally, we represent the normalized sonogram matrix as a sonovector by concatenating the columns. Each normalized sonovector can be viewed as a high-dimensional data point of dimension  $d_s = 7 \times 75 = 525$ .

## 6.4 Clustering of the Reference Set

An essential step of the proposed algorithm is the grouping of the  $\mathcal{R}^{ZNE}$  into several clusters. These will capture the representative patterns in the reference set. Denote this clustering procedure as Reference-Clouds (Ref-Clouds) construction, which is described in Algorithm 1.

---

**Algorithm 1:** Construction of the Reference-Clouds

---

**Input :** The reference set  $\mathcal{R}^{ZNE}$ , the number of clouds K.

**Output:** A set of point clouds  $\{\mathcal{C}_k\}_{k=1}^K$ , their associated centers of masses  $\{m_k\}_{k=1}^K$  and covariance matrices  $\{\Sigma_k\}_{k=1}^K$ .

1. For each input data sample  $r_i(t) = (r_i^Z(t); r_i^N(t); r_i^E(t))$ , concatenate the sonovectors of 3 channels to form a single high-dimensional vector of size  $(3 \times d_s)$ .
  2. Apply the DM on the output of the previous step and construct the DM coordinates  $V(r_i) = (v_1(r_i), v_2(r_i) \dots), \forall r_i \in \mathcal{R}^{ZNE}$ .
  3. Apply k-means to the output in the reduced DM space.
  4. Use the cluster division of Step 3 to form Ref-Clouds  $\{\mathcal{C}_k^Z, \mathcal{C}_k^N, \mathcal{C}_k^E\}_{k=1}^K$  for each channel in the original sonogram space.
  5. For each point cloud and for each channel separately, compute  $m_k$  and  $\Sigma_k$  from  $\mathcal{C}_k$ .
- 

In order to define the Ref-Clouds, the 3-channel sonovectors of size  $d_s$  ( $d_s = 525$  for the current dataset) are first concatenated so that each event is represented by long concatenated sonovectors of size  $3 \cdot d_s$  (respectively, its size is  $3 \times 525 = 1575$  for the current dataset). Then, DM is applied to the long concatenated sonovectors that form the reference set. The first three DM coordinates are selected for forming a reduced representation of  $\mathcal{R}^{ZNE}$ . For the sub-grouping step, the k-means algorithm [93, 94] is applied in the 3-dimensional space of selected DM coordinates. It yields a set of  $K$  point clouds. Next, the indices of the point clouds are matched to their associated high-dimensional reference sonovectors (for each channel separately). Therefore, the original reference set of sonovectors belonging to each channel is

now clustered into  $K$  groups  $\{\mathcal{C}_k^Z, \mathcal{C}_k^N, \mathcal{C}_k^E\}_{k=1}^K$  referred to as Ref-Clouds. Last, two characteristics are computed for each one of the Reference-Clouds (Ref-Clouds) and each channel separately. The point cloud's center of mass and its covariance matrix.

The first characteristic is computed by finding the center of mass of each point cloud in the low-dimensional space. It should be noted that there is no actual sonovector in  $\mathcal{R}^{ZNE}$  that belongs to the center of mass, hence the closest point in the 3-dimensional space is assumed to be a good representative sample for the reference point cloud. Denote by  $m_k$  its corresponding sonovector.

The second characteristic is the covariance matrix, denoted by  $\Sigma_k$ . It can be considered as a local feature, which allows to explore the local tangent spaces to the manifold of each cloud at  $m_k$ . In particular, all of the sonovectors in the Ref-Clouds are used to compute the covariance matrix of size  $d_s \times d_s$ . We remark that each one of the Reference-Clouds (Ref-Clouds) contain a different number of sonovectors (depending on the variability within  $\mathcal{R}^{ZNE}$ ), yet the size of the covariance matrix is fixed and dependents on the size of sonovector,  $d_s$ . Let  $\{m_k^{ZNE}\}_{k=1}^K = \{m_k^Z, m_k^N, m_k^E\}_{k=1}^K$  and  $\{\Sigma_k^{ZNE}\}_{k=1}^K = \{\Sigma_k^Z, \Sigma_k^N, \Sigma_k^E\}_{k=1}^K$  denote the  $K$  characteristics sets.

In Section 6.5, we elaborate on how these two characteristics are used for the construction of the kernel distance.

## 6.5 The training phase

The goal of the training phase is to obtain a representation whose structure separates between samples from the class of interest, and the other samples. The training set  $\mathcal{X}^{ZNE}$  includes sonogram data from both  $\mathcal{R}^{ZNE}$  and  $\mathcal{S}^{ZNE}$ . First, REF-DM is applied to each channel's data separately, based on the output of Algorithm 1. Then, a fused DM representation is formed by concatenating the leading diffusion coordinates from the REF-DM of each channel into a single input vector [2, 75]. Application of DM to this input vector results in a compact representation of the seismic training data. The proposed training procedure is described in Algorithm 2.

Steps 1-5 are repeated three times (once for each channel) in order to compute the REF-DM representation ( see Eqs. (4.1)-(4.7) ). To do so,  $m_k$  and  $\Sigma_k$ , which computed in Algorithm 1 are used. Since the size of each Ref-Clouds is usually

---

**Algorithm 2:** Reference-based Diffusion Maps (REF-DM) Training phase

---

**Input :** Training set  $\mathcal{X}^{ZNE} = \mathcal{R}^{ZNE} \cup \mathcal{S}^{ZNE}$ ,  $\{m_k^{ZNE}\}_{k=1}^K$ ,  $\{\Sigma_k^{ZNE}\}_{k=1}^K$

**Output:** A low dimensional representation of the training data:

$$\Psi^Z(x^Z), \Psi^N(x^N), \Psi^E(x^E), \text{ Fused: } \Psi^{ZNE}(x^{ZNE})$$

**for**  $\mathcal{X}^{ch}$  in  $\{\mathcal{X}^Z, \mathcal{X}^N, \mathcal{X}^E\}$  **do**

- 1. Build an anisotropic kernel by  $A(x^{ch}, k) = \exp \left\{ -\frac{(x^{ch} - m_k^{ch})^T \Sigma_k^{ch \dagger} (x^{ch} - m_k^{ch})}{\epsilon} \right\}$ ,  $0 \leq k \leq K, \forall x \in \mathcal{X}^{ch}$ .
- 2. Normalize by  $\bar{A} = D^{-1} A D_1^{-1}$
- 3. Compute  $\bar{W}_{ref} = \bar{A}^T \bar{A}$
- 4. Compute the spectral decomposition  $\{\phi_l, \lambda_l\}_{l=1}^{K-1}$  of  $\bar{W}_{ref}$ .
- 5. Compute  $\Psi^{ch}(x) = \{\psi_l(x)\}_{l=1}^{l^*}$ , where  $\psi_l = \frac{1}{\lambda_l^{1/2}} \bar{A} \phi_l$ .

**end**

Define each output  $\Psi^{ch}(x)$  of the three iterations of Steps 1-5, as  $\Psi^Z(x^Z)$ ,  $\Psi^N(x^N)$ ,  $\Psi^E(x^E)$ .

- 6. Concatenate the 3 low dimensional representations  $\{\Psi^Z(x^Z), \Psi^N(x^N), \Psi^E(x^E)\}$ .
  - 7. Apply the DM on the output of Step 6, to form a fused low dimensional representation  $\Psi^{ZNE}(x^{ZNE})$ .
- 

smaller than  $d_s$ , the covariance matrix is singular and non-invertible. Consequently, we use its pseudo-inverse. Note, if a sonovector  $s_i \in \mathcal{S}$  is similar to a one of the Reference-Clouds (Ref-Clouds)  $k_j \in \{1,..K\}$ , then the value of  $A(s_i, k_j)$  is higher. When a sonovector  $s_i \in \mathcal{S}$  is similar to many Ref-Clouds, its associated kernel values increase, which yields its corresponding point in the low dimensional  $\Psi^{ch}(x)$ , to be closer to the reference points.

Next, in Steps 6-7, a concatenated DM approach [2] is used to fuse the REF-DM representations of the three channels Z, N, E. In Step 6 we concatenate the REF-DM results into a tensor of size  $N \times (l^* \times 3)$ , where  $N$  is the number of

training samples, and  $l^*$  is the number of the leading kept eigenvalues. Then, DM is applied to this concatenated set. This yields a fused low-dimensional representation  $\Psi^{ZNE}(x^{ZNE})$  of size  $N \times l^*$ . Hence from Step 6 to Step 7 the dimension is essentially reduced.

## 6.6 The test phase

In this section, we described the extension of the low-dimensional representation to include new arrivals.

---

### Algorithm 3: Classification of a new detected arrival

---

**Input :** Detected arrival  $y^{ZNE}$ ,  
 Training set  $\mathcal{X}^{ZNE}$ ,  $\{m_k^{ZNE}\}_{k=1}^K$ ,  $\{\Sigma_k^{ZNE}\}_{k=1}^K$ , eigenpairs  $\{\lambda_l, \phi_l\}_{l=1}^{l^*}$ ,  
 $\Psi^{ZNE}(x^{ZNE})$

**Output:** A low dimensional representation of the detected arrival  $\Psi^{ZNE}(y)$ , a  
 label for the detected arrival

**for**  $y^{ch}$  in  $\{y^Z, y^N, y^E\}$  **do**

- 1. Compute the associated  $K$  distances from the  
 new sample by  $A'(y^{ch}, k) = \exp \left\{ -\frac{(y^{ch} - m_k^{ch})^T \Sigma_k^{ch \dagger} (y^{ch} - m_k^{ch})}{\epsilon} \right\}$ ,  $0 \leq k \leq K$ .
- 2. Normalize by  $\bar{A}' = D^{-1} A D_1^{-1}$
- 3. Compute  $\Psi^{ch}(y) = \{\psi_l(y)\}_{l=1}^{l^*}$ ,  
 using  $\{\lambda_l, \phi_l\}_{l=1}^{l^*}$  from the training phase.

**end**

Define each output  $\Psi^{ch}(y)$  of the three iterations of Steps 1-3, as  $\Psi^Z(y^Z)$ ,  
 $\Psi^N(y^N)$ ,  $\Psi^E(y^E)$ .

- 4. Concatenate the 3 low dimensional representations  
 $\{\Psi^Z(y^Z), \Psi^N(y^N), \Psi^E(y^E)\}$ .
- 5. Apply the geometric harmonics on the output of Step 4, to form a fused  
 low dimensional representation  $\Psi^{ZNE}(y^{ZNE})$ .
- 6. Classify  $\Psi^{ZNE}(y^{ZNE})$  using k-NN.

---

Here, we use  $\{m_k\}_{k=1}^K$ ,  $\{\Sigma_k\}_{k=1}^K$  and  $\{\lambda_d, \phi_d\}_{d=1}^{K^*}$  of the three channels Z, N, E, computed in the training phase. The out-of-sample extension for a new detected arrival  $y \in \mathcal{Y}^{ZNE}$  is presented in Algorithm 3.

Steps 1-3 are repeated three times (once for each channel) in order to compute the REF-DM representation (see equations (4.1)-(4.7)), these equations are modified for the detected arrival  $y$ . Note that in the test phase there is no spectral decomposition, here we use the eigenpairs from the training phase in equation (4.7).

Next, in Steps 4-5, the geometric harmonics are evoked to extend the diffusion coordinates of the concatenated embeddings  $\Psi^{ZNE}(x^{ZNE})$ , which was formed in the training phase. In Step 4 we concatenate the REF-DM results into a tensor of size  $1 \times (l^* \times 3)$ , where 1 indicates the single detected arrival, and  $l^*$  is the number of the leading eigenvalues kept. Then, geometric harmonics are applied using the fused low-dimensional representation  $\Psi^{ZNE}(x^{ZNE})$  of the training set  $\mathcal{X}^{ZNE}$ . This yields a fused low-dimensional representation  $\Psi^{ZNE}(y^{ZNE})$  of the detected arrival size  $1 \times l^*$ .

Finally, in Step 6, the classification step, we find the k-NN of  $\Psi^{ZNE}(y^{ZNE})$  in the fused REF-DM space, using the training labels to determine if the detected arrival belongs to the class of interest or not.

# 7 Experimental Results

This section presents the results of the REF-DM application to the datasets. First, we show that REF-DM produces a stable embedding for  $\mathcal{R}^{ZNE}$  with respect to changing the additional training subset  $\mathcal{S}^{ZNE}$  size. Then, we demonstrate how this embedding captures several intrinsic properties of the reference data. Last, results for the classification of new events using the out-of-sample extension are plotted.

## 7.1 Stability of the Embedding

Figure 7.1 demonstrates the stability of REF-DM with respect to different training sets that hold varied types of data and are of growing size.

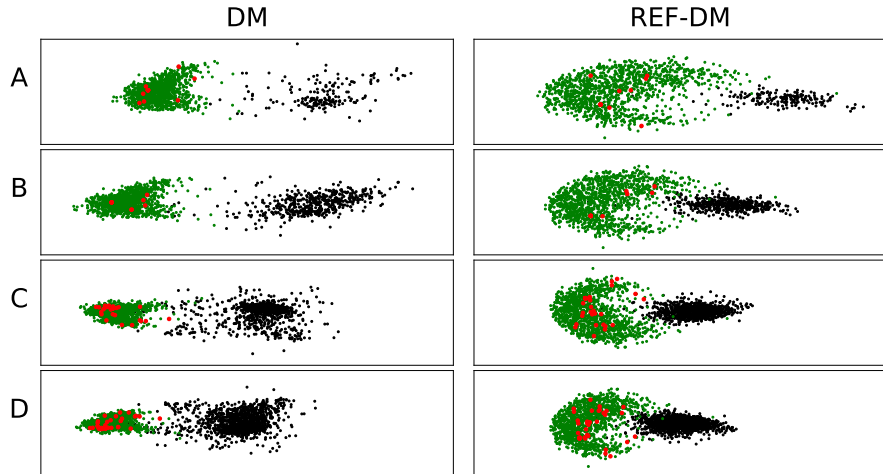


**Figure 7.1:** Training output (of channel E) of Diffusion Maps (DM) versus Reference-based Diffusion Maps (REF-DM) applied to datasets configurations A-D (x-axis and y-axis are the REF-DM coordinates  $\psi_1^Z(x)$  and  $\psi_2^Z(x)$ , respectively).

In these plots, we compare channel E’s training output of DM (first column) to the training output of REF-DM (second column). Rows A-D indicates four different datasets configurations (see Table 6.1), where the size of  $\mathcal{S}^{ZNE}$  increases from top to bottom. The entire reference set is contained in all datasets configurations, where its embedded points appear as the green points. The other points indicate the embeddings of  $\mathcal{S}^{ZNE}$ , where the red points belong to the class of interest (Eshidiya mine) and the black points do not. The axes of all sub-figures present the diffusion coordinates  $\psi_2^Z(x)$  and  $\psi_4^Z(x)$ , while their scales are similar.

By comparing the first row (small training set) to the fourth row (large training set), it is apparent in the left column that REF-DM’s geometric structure of the green cluster, corresponding to the class of interest, is preserved. However, it is noticeable in the right column, that DM’s geometric structure of the green cluster is unstable across rows and is heavily influenced by the size of the training set and the balance of positive and negative samples within it. Hence, the proposed algorithm’s embeddings are much more steady and robust to changes in the training set’s size than the DM’s embeddings.

## 7.2 Intrinsic Organization of the Mine Blasts Set

The high-dimensional data is governed by several intrinsic parameters, such as the blast location, its yield, and the blasting procedure. Those parameters, however, are unknown in the absence of ground truth data. On the other hand, there is estimated parametric information about the waveforms contained in the GII seismic catalog. The estimation of the blast location is defined by the first and second available parameters: latitude (LAT) and longitude (LON) . The third one is the duration magnitude (Md). The fourth parameter is the event’s normalized age (Aging). The time difference between the explosion origin time by GII and the first sample time of each waveform is the fifth parameter (dTime).

Figure 7.2 presents the training output of Algorithm 2 on dataset configuration C of channel Z, colored by the different properties. To generate a clearer picture, only the reference set’s embedded points set are plotted. As can be seen, in the left sub-figure, only the green cluster of the class of interest, which was earlier shown in Figure 7.1 is presented here in all three sub-figures. The axes in all sub-figures are chosen to be  $\psi_2^Z(x)$  and  $\psi_4^Z(x)$ , because the second and fourth REF-DM coordinates are the most correlated with the majority of the available parameters

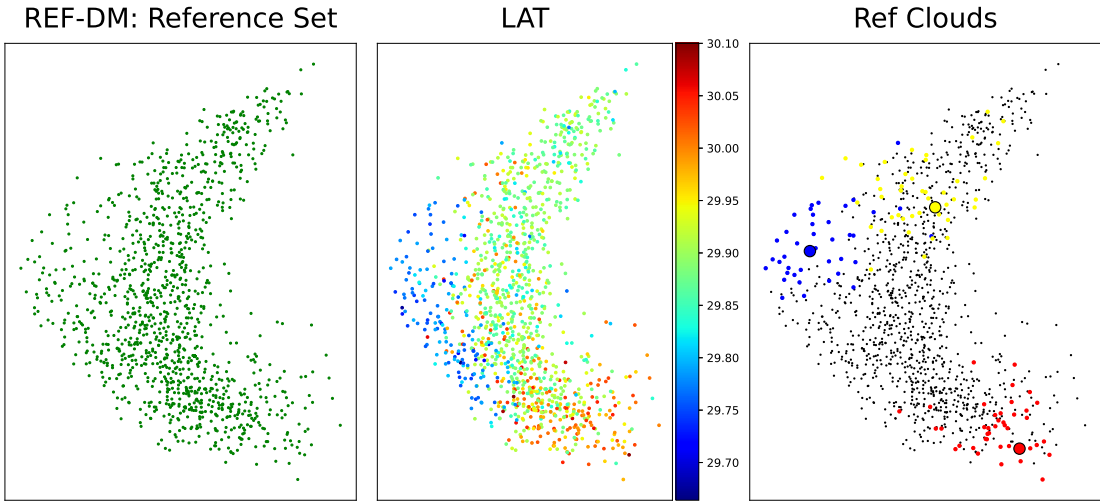


**Figure 7.2:** The reference set’s embedding computed by Algorithm 2 is presented in all three sub-figures (the x-axis and y-axis are the REF-DM coordinates  $\psi_4^Z(x)$  and  $\psi_2^Z(x)$ , respectively). Left: The embedding points of the reference set are displayed here as the green cluster of the class of interest, as similarly illustrated earlier in Figure 7.1. Middle: the same points but colored by the LAT value of each event. Right: three example point-clouds that were computed in the reference clustering procedure (Algorithm 1).

(according to Table 7.1). In the middle, the reference set’s embedding is colored by each point’s LAT value.

It can be seen in the middle subplot of Figure 7.2, that events with the higher LAT values (red) are mapped to the right bottom part of the REF-DM embedding. Events with the lower LAT values (blue) are mapped to the left middle part of the REF-DM embedding. Hence, there is a correlation between the LAT values and  $\psi_4^Z(x)$ , the REF-DM coordinate on the vertical axis, which corresponds to the relatively high correlation value in Table 7.1, first row on the right.

Figure 7.2 (right) shows the clustering of the reference set into  $K = 20$  point-clouds. Only 3 representative point-clouds (clouds numbers 5, 13, and 14) are colored (regardless of the coloring of the LAT values) to show the compatibility between the Reference-Clouds (Ref-Clouds)’ structure and an intrinsic parameter of the dataset. The three larger points are the centers of mass of the colored clouds.

Table 7.1 contains the Spearman’s rank correlation coefficient and its associated p-values between each of the GII seismic catalog’s parameters (LAT, LON, Md, Aging, dTime) and the first four REF-DM coordinates ( $\psi_1^Z(x)$ ,  $\psi_2^Z(x)$ ,  $\psi_3^Z(x)$ ,

$\psi_4^Z(x)$ ). It assesses how well the relationship between them can be described using a monotonic function. In accordance with the demonstration in Figure 7.2, the highest correlation coefficient is between the LAT parameter and  $\psi_4^Z(x)$ .

**Table 7.1: Spearman’s correlation coefficients and computed p-values between the five available GII seismic catalog’s parameters and the first four REF-DM coordinates (dataset configuration C, channel Z).**

	REF-DM $\psi_1^Z(x)$	REF-DM $\psi_2^Z(x)$	REF-DM $\psi_3^Z(x)$	REF-DM $\psi_4^Z(x)$
	correlation/p-value	correlation/p-value	correlation/p-value	correlation/p-value
LAT	-0.053, 6.2e-2	-0.277, 1.6e-22	-0.106, 2.0e-4	-0.358, 1.3e-37
LON	0.083, 3.6e-3	0.083, 3.8e-3	0.152, 1.1e-07	0.294, 2.5e-25
Md	-0.225, 2.9e-15	0.296, 1.0e-25	-0.274, 4.2e-22	-0.014, 6.1e-1
Aging	0.116, 5e-05	-0.050, 8.2e-2	0.229, 1.0e-15	0.168, 4.8e-09
dTime	0.106, 2.3e-4	-0.341, 3.9e-34	0.090, 1.6e-3	0.139, 1.3e-06

Next, we demonstrate how each point-cloud captures slightly different groups of Eshidiya mine explosion events. The first row of Figure 7.3 displays three normalized sonograms of channel Z belonging to different Ref-Clouds of the reference set. For each normalized sonogram, time is represented along the x-axis from left to right, ad frequency is represented along the y-axis from top to bottom. These events are the clouds’ centers of mass from Figure 7.2, marked as the larger blue, yellow, and red circles, with black edges, respectively.

These normalized sonograms are representative examples of templates from the reference set, which demonstrate how time-frequency features vary between the recorded events. The left bright lines on the left sides of all normalized sonograms are associated with the P-waves while the S-waves are expressed in the center of the sonograms. In general, the patterns of all three sonograms correspond to mine explosions based on the P-waves and S-waves features, as well as the distance between them, although there is some variability between them.

On the other hand, notice that the brightest P-waves features (left bright lines, i.e. features with high energy content) of each one of the Ref-Clouds’s sonograms have slightly different patterns (see Figure 7.3, markings B1-2,Y1-2,R1). Similarly, it can be seen for the S-waves features in the sonograms’ center (see for example marking R2).

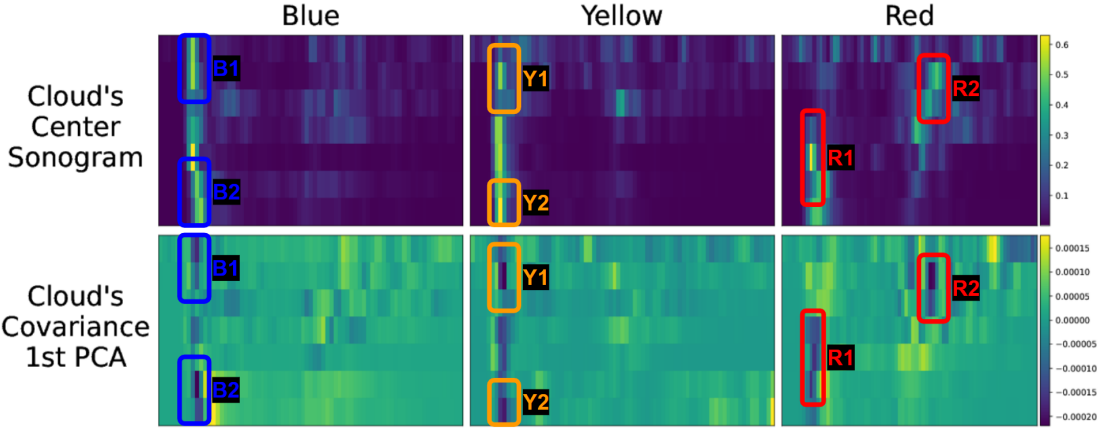


**Figure 7.3:** An example of the two characteristics of each of the three colored Ref-Clouds showed in Figure 7.2. The columns are arranged in the order of the clouds: blue, yellow, and red. In the first row, the normalized sonograms (of channel Z) of the center of mass of each point-cloud are shown. In the second row, the first PCA of the covariance matrix characterizes each point-cloud is presented. The markings B1-2, Y1-2, R1-2 denote the features that most characterize each point-cloud and are shared by all sonograms in it (according to the connection between each pair of markings in each column).

For our seismic application, the variability within the reference set is can be visually observed in Figure 7.3 by the varying characteristics between the distinct Ref-Clouds. Because of this variability, a single template is not suitable for detecting all of the blasts in the given reference set. This issue was also studied by [49] on this same dataset. They picked a small subset of signals having the highest similarity to all other signals. Thus, using the multiple-templates approach is more appropriate for this type of varied, one-class classification.

Visualization of the variance within each the Ref-Clouds is a useful analysis tool. To do so, the covariance matrix of each set of sonovectors is computed. Then, its first PCA is calculated. In the second row of Figure 7.3, its per-feature empirical mean is plotted three times, each belongs to one of the three clouds from Figure 7.2. In each column, the cloud's center of mass sonogram and the corresponding cloud's covariance first PCA are plotted.

To distinguish between the Ref-Clouds, markings B1-2,Y1-2,R1-2 are used in each column of 7.3. These features were chosen to be marked because they are the darkest features in the bottom row, indicating that the variance between these features

in each point-cloud's sonograms is low. By comparing the columns, the variability between the Ref-Clouds can be seen. For example, markings B1-2 highlight the common characteristics of the blue cloud, which are very low-frequencies P-wave (B1) and very high-frequencies S-wave (B2). For the yellow cloud, markings Y1-2 denoted a slightly different pattern of the P-wave. On the other hand, for the red cloud, R1 denotes the middle-high frequencies of the P-wave, while R2 denotes the low-middle frequencies of the S-wave.

### 7.3 Classification Outcome

Figure 7.4 plots the results of the training phase of REF-DM of channels Z, N, E, and their fusion, using different training set configurations (see Table 6.1), as produced by Algorithm 2. The columns plots the first two REF-DM coordinates:  $\{\psi_1^Z(x), \psi_2^Z(x)\}$ ,  $\{\psi_1^N(x), \psi_2^N(x)\}$ ,  $\{\psi_1^E(x), \psi_2^E(x)\}$ , and  $\{\psi_1^{ZNE}(x), \psi_2^{ZNE}(x)\}$ . All sub-plots have the same axis scales, except for the fourth column which changes due to the additional fusion DM in Step 7 of Algorithm 2.

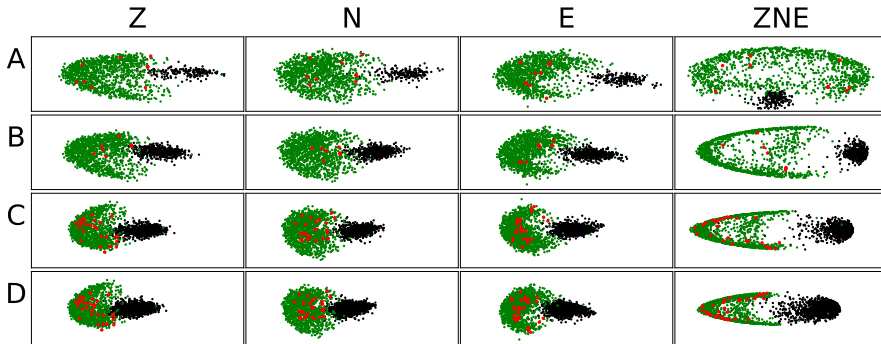


**Figure 7.4: Results of Algorithm 2.** The columns are arranged according to the channels as follows: Z, N, E and their fusion, from left to right. The rows are arranged according to the datasets configurations: A, B, C, D, from top to bottom.

It can be seen how REF-DM robustly handles the increasing size of the additional training subset. Examining each column from top to bottom reveals that REF-DM's geometric structure of the green cluster corresponding to the class of interest is preserved.

Notice that as the size of the training set increases, the *positive class* becomes more stable. By distinguishing between the difference in the cluster's geometric

structure in the first and second rows and comparing it to the difference between the third and fourth rows.

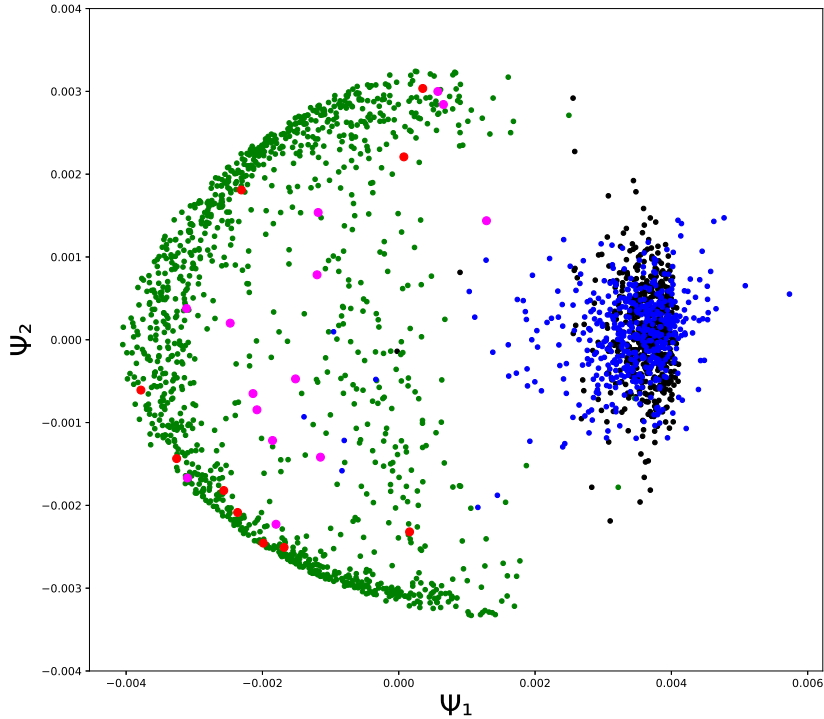
The fused embedding in the fourth column separates the positive and the negative classes, without losing details. Although Figure 7.4 shows only the first two dimensions of the training embeddings, in Algorithm 3 the classification is based on  $l^*$  dimensions of the training embeddings. The first row in Figure 7.4 plots the results of dataset configuration A, which contains an additional training subset of only 190 arrivals, which causes some instability in the clusters. When compared to the other rows, this is noticeable by the large positive cluster in the first row. Nevertheless, even in the first row, the red points are embedded in the cluster of the correct class (see also Figure 7.6). Thus, even for a small training set, the classification accuracy of REF-DM on the training set is very high. The results of Algorithm 2 yield very good classification, especially the fused REF-DM in the fourth column, as it well separates between the positive and negative classes.

Figure 7.5 plots the first two embedding coordinates of the out-of-sample extension  $\Psi^{ZNE}(y)$ , which are the output of Algorithm 3, for the first test set  $\mathcal{Y}_1^{ZNE}$ . Additionally, the first two coordinates of the training set's embedding  $\Psi^{ZNE}(x)$ , which are the output of Algorithm 2 are plotted.

The test points that belong to the class of interest are colored in pink. It can be seen that all of them were successfully mapped into the positive class. The test points that do not belong to the Eshidiya mine are colored in blue. Most of them are mapped to the negative class, where the black training points are located. However, several test points are falsely embedded in the positive cluster. From the CTBTO's point of view, these points are denoted as false alarms and may be manually checked. It should be noted that the proposed algorithm has attributed several CTBTO arrivals to the positive class that wasn't reported by the GII catalog (GII is not obliged to report all explosions at the Eshidiya mine).

In addition, the manual analysis using additional seismic stations in Israel's national seismic network confirmed that these arrivals actually have wrong labels, i.e. they originated from blasts at the Eshidiya mine.

Table 7.2 presents the confusion matrices computed from the classification results of Algorithm 3. Each row of the confusion matrices represents the events in an actual class while each column represents the events in a predicted class. The model was trained on dataset configuration A and tested on two different test sets  $\mathcal{Y}_1^{ZNE}$  and  $\mathcal{Y}_2^{ZNE}$ . Classification of the label for each test point is performed



**Figure 7.5:** Results of Algorithm 3 plotted by the first two REF-DM coordinates of the training and test sets. The black and blue points belong to the events with the negative label from the training set and test set, respectively. The green points belong to the events from the reference set. The red and pink points belong to the events with the positive label from the training set and test set, respectively.

using a k-NN classifier, with  $k = 21$ . It can be seen that the fused REF-DM coordinates  $\Psi^{ZNE}$  resulted in the lowest number of false-positive classifications than each channel individually. Thus, the fused representation improves the one-channel classification.

Table 7.3 shows the classification results of the fused representations of the three channels Z, N, E, and compares the classical DM and REF-DM. In The first column, DM resulted with 47 false-positive classifications for the first test set  $\mathcal{Y}_1^{ZNE}$ . For the second test set  $\mathcal{Y}_2^{ZNE}$ , DM resulted in 19 false-positive classifications. On the other side, REF-DM obtained 7 false-positive classifications for the first test set  $\mathcal{Y}_1^{ZNE}$  and 5 for  $\mathcal{Y}_2^{ZNE}$ . Our proposed model achieved a better classification rate.

For our particular application, false-negative events would be preferred over false-

**Table 7.2:** Classification results of Algorithm 3 presented by confusion matrices.

TP FP	FN TN	$\mathcal{Y}_1^{ZNE}$	$\mathcal{Y}_2^{ZNE}$
$\Psi^Z$	18 17	0 810	5 13
			0 474
$\Psi^N$	18 20	0 809	5 34
			0 453
$\Psi^E$	18 19	0 808	5 23
			0 464
$\Psi^{ZNE}$	17 7	1 820	5 <b>5</b>
			0 482

positive ones. Because it will be desirable for global nuclear explosion monitoring systems if minor mine explosions are already masked out at the single-station automatic processing level. As a result, if false-positive events are automatically masked out, suspicious events may go undetected.

**Table 7.3:** The comparison between the fused representations of the classical DM (left column) and REF-DM (right column).

TP FP	FN TN	DM	REF-DM
$\mathcal{Y}_1^{ZNE}$	18 47	0 780	17 <b>7</b>
			1 820
$\mathcal{Y}_2^{ZNE}$	5 19	0 468	5 <b>5</b>
			0 482

Figure 7.6 plots the algorithms' accuracy values as a function of the number of training days of the additional training subset, where dataset configuration C (Table 6.1) had been used. Hence, the model was trained several times with an increasing number of days, where the test set included the complementary decreasing number of days left from the dataset of March 2011. For each of the 16 days in the figure, the average number of events is 38.68, with a standard deviation of 45.60. The blue lines indicate the DM results, and the red line indicates the REF-DM

results. It is interesting to see that the red bold line (fused REF-DM) reaches a high accuracy very fast, and it is above the other lines until they reach a saturation point, in which there are enough training samples for all methods. Except for the reference set, REF-DM requires just three additional training days to obtain 99% accuracy, but DM requires at least ten. Thus, an important advantage in this application is that the fused REF-DM model doesn't require a lot of samples to reach very high accuracy, here, an additional training subset from a single day is sufficient.

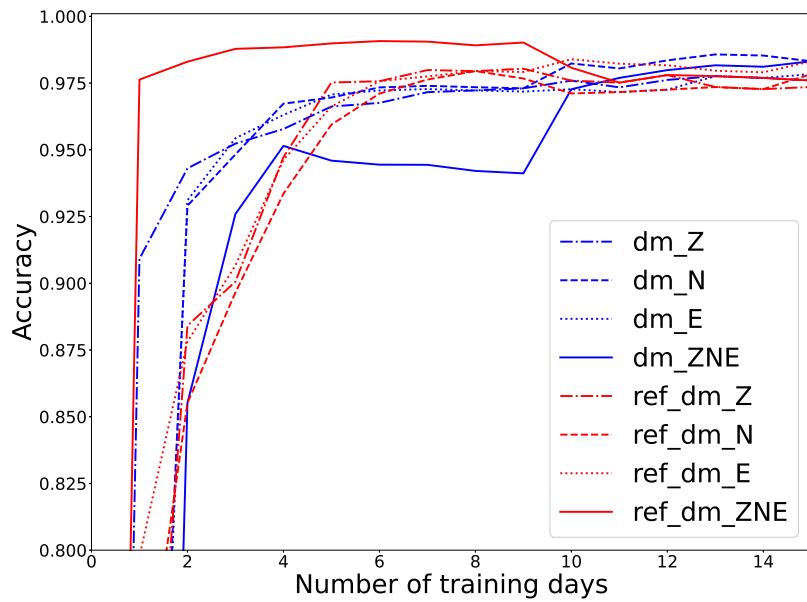


**Figure 7.6: Classification Accuracy as function of number of training stream days, where 6 different representation were used. The bold lines belong to the fused diffusion coordinates.**

### 7.3.1 Comparison with deep learning methods

In this section, the proposed REF-DM algorithm is compared with deep learning methods. Convolutional neural networks (CNNs) with a simple architecture have difficulty extracting high dimensional abstract data features and may result in an under-fitting model. As a consequence, model-based transfer learning was used in this work to obtain efficient data feature extraction and classification. Previous research has found that the bottom layer features do not appear to be specific to

a particular dataset or task, but rather are general to different datasets and tasks. The top layer features, on the other hand, are more specific [95].

In this experiment, the bottom transferred layers of the pre-trained deep neural networks were frozen for general feature extraction, except for the last fully-connected layer which was fine-tuned to extract specific features in this task. VGG16 [60], EfficientNet B4-5 [61], ResNet18-50 [62], and Inception-v3 [63] are widely used pre-trained deep neural networks. These networks were examined in this paper.

The deep learning framework was built with PyTorch [96], and trained using Google Colab’s GPU. As an outcome of hyper-parameter tuning, the following parameters were chosen: batch size = 32, learning rate = 0.001, weight decay = 0.001. In addition, Adam optimizer [97] and cross-entropy loss function were used.

EfficientNet, ResNet, and Inception were the pre-trained deep neural networks whose outcomes were the least accurate, with less than 89% accuracy rate. It may be possible to optimize the results of these networks by using more sophisticated training methods and architectural modifications.

VGG16 outperformed the other networks we examined. Its architecture includes a series of convolutional and max-pooling layers, followed by three fully-connected layers at the end. We modified the last fully-connected layer as a fixed feature extractor to classify two classes (positive and negative) in the test sets. The number of epochs that produce the best outcomes is 5.

The training set  $\mathcal{X}^{ZNE}$  (configuration A) and the test sets are  $\mathcal{Y}_1^{ZNE}$ ,  $\mathcal{Y}_2^{ZNE}$  are shaped into the shape that the pre-trained model expects. For VGG16, each sonovector is arranged back into a 2D sonogram of size  $7 \times 75$ . The remaining pixels were padded with zeros. The three channels were concatenated to a final input matrix of size  $3 \times 224 \times 224$ . VGG16 achieved 97.04% test accuracy for  $\mathcal{Y}_1^{ZNE}$ , and 97.76% test accuracy for  $\mathcal{Y}_2^{ZNE}$ . Notice, that practically we have used  $\mathcal{Y}_1^{ZNE}$  as a validation set. REF-DM, on the other hand, achieved 99.05% test accuracy for  $\mathcal{Y}_1^{ZNE}$  and 98.98% test accuracy for  $\mathcal{Y}_2^{ZNE}$  (calculated according to Table 7.3).

To conclude, when comparing to the classification results in Section 7.3, VGG16 outperformed the standard DM, although REF-DM still outperformed it.

## 8 Conclusions And Future Work

We proposed to model an OCC problem using a method called Reference-based Diffusion Maps (REF-DM) using anisotropic diffusion methods. To demonstrate the advantages of the proposed method, a novel application is developed for modeling an ensemble of seismic events, of a specific target class, related by a common signal-space geometry. We perform automatic identification of mine explosions that originate from a specific mine, given a stream of seismic data. Its capability to screen out a diversity of seismic events, such as earthquakes, explosions of different mines, and background signals, is successfully demonstrated on several large datasets. Its associated events were detected by Comprehensive Nuclear Test Ban Treaty Origination and labeled by Israel National Data Center experts and compared with deep learning techniques. The proposed framework includes a preliminary offline procedure of Ref-Clouds construction, training phase, and test phase.

The pre-fixed historical reference set is clustered into number point-clouds of samples, which correspond to similar underlying parameters representing local variability within the class of interest. Then, using an anisotropic kernel, the pairwise distances of the whole training set are calculated considering the local geometry around each sample in the observable space. The unsupervised training phase allowed us to efficiently obtain a compact low dimensional representation, whose structure distinguishes between samples of the class of interest, and the other samples. This approach yields a less distorted embedded representation of the data while preserving the geometry of the physical-space and its intrinsic parameters. For newly arriving samples, the test phase generates an efficient OOSE of the REF-DM embedding coordinates. According to our results, more than 99% of new mine explosions were correctly identified. Therefore, incorporating our application in operational stations may dramatically reduce the analysts' burden.

The method exhibits four key contributions. Firstly, the variability within the

class of interest is captured by locally preserving the geometric structures of its sub-clustered clouds. This allows better visualization, monitoring, and understanding of the inspected phenomena. Additionally, there is no need for a traditional template-selection procedure because the whole set of reference samples is used via data-driven modeling. Secondly, it is robust to the selection of different training sets, compared to classical DM methods. Thirdly, the method offers a simple way for fusing the embedded representations of the 3-channel seismic recordings that capture the data stream, thereby improving the classification. Last, the proposed reference-based out-of-sample extension (OOSE) of newly arriving samples is calculated in an online manner and at a low computational cost.

For future work, developing an end-to-end pipeline for seismic applications is a sought-after follow-up study. It can be done by employing the proposed method for online identification, the input of which is a raw continuous stream data recording. The aim would be to only identify the events of the class of interest in a sequential manner, with a fully automatic framework (without relying on any detector). Also, the spectral ratio [98] is another physical parameter to study to see if it organizes the proposed embedding and correlated to. It is the energy ratio between P-phase and S-phase at various frequencies, which is calculated to discriminate between explosions and earthquakes. Furthermore, extending our approach from a single seismic station to a multi-station network is an intriguing research topic.

The proposed reference-based manifold learning method may be adapted to other types of pattern recognition applications, such as speech recognition, computer vision, and bioinformatics. For example, the decoding of neural data in the human auditory and visual systems. As mentioned, our modeling method may be implemented sequentially, and therefore applicable to a variety of online signal processing tasks.

## 9 Publication and Code Implementation

An article on this work has been published in:

I. Niv, Y. Bregman and N. Rabin, "Identification of Mine Explosions Using Manifold Learning Techniques," in IEEE Transactions on Geoscience and Remote Sensing, vol. 60, pp. 1-13, 2022, Art no. 5912313, doi: 10.1109/TGRS.2022.3153520.

In addition, the code implementation of this work are available at:

[GitHub repository](#).

# Bibliography

- [1] D. B. Harris and D. A. Dodge, “The geometry of signal space: a case study of direct mapping between seismic signals and event distribution,” *Geophysical Journal International*, vol. 224, no. 3, pp. 2189–2208, 2021.
- [2] N. Rabin and A. Averbuch, “Detection of anomaly trends in dynamically evolving systems,” in *2010 AAAI Fall Symposium Series*, 2010.
- [3] R. R. Coifman and S. Lafon, “Diffusion maps,” *Applied and computational harmonic analysis*, vol. 21, no. 1, pp. 5–30, 2006.
- [4] W. Lian, R. Talmon, H. Zaveri, L. Carin, and R. Coifman, “Multivariate time-series analysis and diffusion maps,” *Signal Processing*, vol. 116, pp. 13–28, 2015.
- [5] A. D. Szlam, M. Maggioni, and R. R. Coifman, “Regularization on graphs with function-adapted diffusion processes.,” *Journal of Machine Learning Research*, vol. 9, no. 8, 2008.
- [6] A. Singer, Y. Shkolnisky, and B. Nadler, “Diffusion interpretation of nonlocal neighborhood filters for signal denoising,” *SIAM Journal on Imaging Sciences*, vol. 2, no. 1, pp. 118–139, 2009.
- [7] Y. Keller, R. R. Coifman, S. Lafon, and S. W. Zucker, “Audio-visual group recognition using diffusion maps,” *IEEE Transactions on Signal Processing*, vol. 58, no. 1, pp. 403–413, 2009.
- [8] X. Shen and F. G. Meyer, “Analysis of event-related fmri data using diffusion maps,” in *Biennial international conference on information processing in medical imaging*, pp. 652–663, Springer, 2005.

- [9] F. G. Meyer and X. Shen, “Classification of fmri time series in a low-dimensional subspace with a spatial prior,” *IEEE transactions on medical imaging*, vol. 27, no. 1, pp. 87–98, 2007.
- [10] T. Sipola, F. Cong, T. Ristaniemi, V. Alluri, P. Toiviainen, E. Brattico, and A. K. Nandi, “Diffusion map for clustering fmri spatial maps extracted by independent component analysis,” in *2013 IEEE international workshop on machine learning for signal processing (MLSP)*, pp. 1–6, IEEE, 2013.
- [11] I. K. Gallos, E. Galaris, and C. I. Siettos, “Construction of embedded fmri resting-state functional connectivity networks using manifold learning,” *Cognitive neurodynamics*, vol. 15, no. 4, pp. 585–608, 2021.
- [12] S. Gao, G. Mishne, and D. Scheinost, “Nonlinear manifold learning in functional magnetic resonance imaging uncovers a low-dimensional space of brain dynamics,” *Human brain mapping*, 2021.
- [13] W. Lian, R. Talmon, H. Zaveri, L. Carin, and R. Coifman, “Multivariate time-series analysis and diffusion maps,” *Signal Processing*, vol. 116, pp. 13–28, 2015.
- [14] A. Singer and R. R. Coifman, “Non-linear independent component analysis with diffusion maps,” *Applied and Computational Harmonic Analysis*, vol. 25, no. 2, pp. 226–239, 2008.
- [15] A. Singer, R. Erban, I. G. Kevrekidis, and R. R. Coifman, “Detecting intrinsic slow variables in stochastic dynamical systems by anisotropic diffusion maps,” *Proceedings of the National Academy of Sciences*, vol. 106, no. 38, pp. 16090–16095, 2009.
- [16] D. Kushnir, A. Haddad, and R. R. Coifman, “Anisotropic diffusion on sub-manifolds with application to earth structure classification,” *Applied and Computational Harmonic Analysis*, vol. 32, no. 2, pp. 280–294, 2012.
- [17] A. Haddad, D. Kushnir, and R. R. Coifman, “Texture separation via a reference set,” *Applied and Computational Harmonic Analysis*, vol. 36, no. 2, pp. 335–347, 2014.

- [18] R. Talmon, I. Cohen, S. Gannot, and R. R. Coifman, “Supervised graph-based processing for sequential transient interference suppression,” *IEEE transactions on audio, speech, and language processing*, vol. 20, no. 9, pp. 2528–2538, 2012.
- [19] R. Talmon and R. Coifman, “Intrinsic modeling of stochastic dynamical systems using empirical geometry,” *Applied and Computational Harmonic Analysis*, vol. 39, pp. 138–160, 2015.
- [20] R. Bhattacharya and V. Patrangenaru, “Statistics on manifolds and landmarks based image analysis: A nonparametric theory with applications,” *Journal of Statistical Planning and Inference*, vol. 145, pp. 1–22, 2014.
- [21] D. N. Kaslovsky and F. G. Meyer, “Non-asymptotic analysis of tangent space perturbation,” *Information and Inference: a Journal of the IMA*, vol. 3, no. 2, pp. 134–187, 2014.
- [22] P. Perera and V. M. Patel, “Learning deep features for one-class classification,” *IEEE Transactions on Image Processing*, vol. 28, no. 11, pp. 5450–5463, 2019.
- [23] P. Perera, P. Oza, and V. M. Patel, “One-class classification: A survey,” *arXiv preprint arXiv:2101.03064*, 2021.
- [24] E.-S. Platzer, H. Süße, J. Nägele, K.-H. Wehking, and J. Denzler, “On the suitability of different features for anomaly detection in wire ropes,” in *International Conference on Computer Vision, Imaging and Computer Graphics*, pp. 296–308, Springer, 2009.
- [25] C. M. Bishop, “Pattern recognition,” *Machine learning*, vol. 128, no. 9, 2006.
- [26] M. Kemmler, E. Rodner, E.-S. Wacker, and J. Denzler, “One-class classification with gaussian processes,” *Pattern recognition*, vol. 46, no. 12, pp. 3507–3518, 2013.
- [27] D. M. Tax and R. P. Duin, “Support vector data description,” *Machine learning*, vol. 54, no. 1, pp. 45–66, 2004.

- [28] Q. Leng, H. Qi, J. Miao, W. Zhu, and G. Su, “One-class classification with extreme learning machine,” *Mathematical problems in engineering*, vol. 2015, 2015.
- [29] F. Dufrenois and J.-C. Noyer, “A null space based one class kernel fisher discriminant,” in *2016 international joint conference on neural networks (IJCNN)*, pp. 3203–3210, IEEE, 2016.
- [30] P. Samangouei and R. Chellappa, “Convolutional neural networks for attribute-based active authentication on mobile devices,” in *2016 IEEE 8th International Conference on Biometrics Theory, Applications and Systems (BTAS)*, pp. 1–8, IEEE, 2016.
- [31] U. Mahbub, S. Sarkar, V. M. Patel, and R. Chellappa, “Active user authentication for smartphones: A challenge data set and benchmark results,” in *2016 IEEE 8th international conference on biometrics theory, applications and systems (BTAS)*, pp. 1–8, IEEE, 2016.
- [32] P. Vincent, H. Larochelle, Y. Bengio, and P.-A. Manzagol, “Extracting and composing robust features with denoising autoencoders,” in *Proceedings of the 25th international conference on Machine learning*, pp. 1096–1103, 2008.
- [33] R. Hadsell, S. Chopra, and Y. LeCun, “Dimensionality reduction by learning an invariant mapping,” in *2006 IEEE Computer Society Conference on Computer Vision and Pattern Recognition (CVPR’06)*, vol. 2, pp. 1735–1742, IEEE, 2006.
- [34] P. Vincent, H. Larochelle, I. Lajoie, Y. Bengio, P.-A. Manzagol, and L. Bottou, “Stacked denoising autoencoders: Learning useful representations in a deep network with a local denoising criterion.,” *Journal of machine learning research*, vol. 11, no. 12, 2010.
- [35] D. P. Kingma and M. Welling, “Auto-encoding variational bayes,” *arXiv preprint arXiv:1312.6114*, 2013.
- [36] B. Song, P. Li, J. Li, and A. Plaza, “One-class classification of remote sensing images using kernel sparse representation,” *IEEE Journal of Selected Topics in*

*Applied Earth Observations and Remote Sensing*, vol. 9, no. 4, pp. 1613–1623, 2016.

- [37] S. Gidaris, P. Singh, and N. Komodakis, “Unsupervised representation learning by predicting image rotations,” *arXiv preprint arXiv:1803.07728*, 2018.
- [38] I. Golan and R. El-Yaniv, “Deep anomaly detection using geometric transformations,” *arXiv preprint arXiv:1805.10917*, 2018.
- [39] P. Oza and V. M. Patel, “Active authentication using an autoencoder regularized cnn-based one-class classifier,” in *2019 14th IEEE International Conference on Automatic Face & Gesture Recognition (FG 2019)*, pp. 1–8, IEEE, 2019.
- [40] Y. Baweja, P. Oza, P. Perera, and V. M. Patel, “Anomaly detection-based unknown face presentation attack detection,” in *2020 IEEE International Joint Conference on Biometrics (IJCB)*, pp. 1–9, IEEE, 2020.
- [41] P. Bergmann, M. Fauser, D. Sattlegger, and C. Steger, “Uninformed students: Student-teacher anomaly detection with discriminative latent embeddings,” in *Proceedings of the IEEE/CVF Conference on Computer Vision and Pattern Recognition*, pp. 4183–4192, 2020.
- [42] Z. Zhang, S. Chen, and L. Sun, “P-kdgan: Progressive knowledge distillation with gans for one-class novelty detection,” *arXiv preprint arXiv:2007.06963*, 2020.
- [43] Q. Kong, D. T. Trugman, Z. E. Ross, M. J. Bianco, B. J. Meade, and P. Gerstoft, “Machine learning in seismology: Turning data into insights,” *Seismological Research Letters*, vol. 90, no. 1, pp. 3–14, 2019.
- [44] J. Coyne, D. Bobrov, P. Bormann, E. Duran, P. Grenard, G. Haralabus, I. Kitov, and Y. Starovoit, “Ctbto: Goals, networks, data analysis and data availability,” in *New manual of seismological observatory practice 2 (NMSOP-2)*, pp. 1–41, Deutsches GeoForschungsZentrum GFZ, 2012.
- [45] R. J. Geller and C. S. Mueller, “Four similar earthquakes in central california,” *Geophysical Research Letters*, vol. 7, no. 10, pp. 821–824, 1980.

- [46] D. B. Harris, “A waveform correlation method for identifying quarry explosions,” *Bulletin of the Seismological Society of America*, vol. 81, no. 6, pp. 2395–2418, 1991.
- [47] G. Leonard, M. Villagran, M. Joswig, Y. Bartal, N. Rabinowitz, and A. Saya, “Seismic source classification in israel by signal imaging and rule-based coincidence evaluation,” *Bulletin of the Seismological Society of America*, vol. 89, no. 4, pp. 960–969, 1999.
- [48] J. K. MacCarthy, H. Hartse, M. Greene, and C. Rowe, “Using waveform cross-correlation and satellite imagery to identify repeating mine blasts in eastern kazakhstan,” *Seismological Research Letters*, vol. 79, no. 3, pp. 393–399, 2008.
- [49] Y. Ben Horin, D. Bobrov, I. Kitov, M. Rozhkov, and M. Yedlin, “The use of waveform cross correlation for detection, relative location and magnitude estimation of repeated mining blasts: the jordan phosphate mine eshidiya, *CTBT: Science and Technology 2015 Conference*, 2017, vienna, poster.”
- [50] D. Harris and D. Dodge, “An autonomous system for grouping events in a developing aftershock sequence,” *Bulletin of the Seismological Society of America*, vol. 101, no. 2, pp. 763–774, 2011.
- [51] A. Aguiar, D. Dodge, and S. Myers, “The application of a dynamic correlation processor for international monitoring system, *CTBT: Science and Technology 2021 Conference*, 2021, vienna, poster, p3.5-198..”
- [52] L. Linville, K. Pankow, and T. Draelos, “Deep learning models augment analyst decisions for event discrimination,” *Geophysical Research Letters*, vol. 46, no. 7, pp. 3643–3651, 2019.
- [53] K. M. Taylor, M. J. Procopio, C. J. Young, and F. G. Meyer, “Estimation of arrival times from seismic waves: a manifold-based approach,” *Geophysical Journal International*, vol. 185, no. 1, pp. 435–452, 2011.
- [54] J. Ramirez Jr and F. G. Meyer, “Machine learning for seismic signal processing: Phase classification on a manifold,” in *2011 10th international conference on machine learning and applications and workshops*, vol. 1, pp. 382–388, IEEE, 2011.

- [55] N. Rabin, Y. Bregman, O. Lindenbaum, Y. Ben-Horin, and A. Averbuch, “Earthquake-explosion discrimination using diffusion maps,” *Geophysical Journal International*, vol. 207, no. 3, pp. 1484–1492, 2016.
- [56] O. Lindenbaum, Y. Bregman, N. Rabin, and A. Averbuch, “Multiview kernels for low-dimensional modeling of seismic events,” *IEEE Transactions on Geoscience and Remote Sensing*, vol. 56, no. 6, pp. 3300–3310, 2018.
- [57] O. Lindenbaum, N. Rabin, Y. Bregman, and A. Averbuch, “Seismic event discrimination using deep cca,” *IEEE Geoscience and Remote Sensing Letters*, vol. 17, no. 11, pp. 1856–1860, 2019.
- [58] Y. Bregman, O. Lindenbaum, and N. Rabin, “Array based earthquakes-explosion discrimination using diffusion maps,” *Pure and Applied Geophysics*, 2020.
- [59] Y. Bregman and N. Rabin, “Aftershock identification using diffusion maps,” *Seismological Research Letters*, vol. 90, no. 2A, pp. 539–545, 2019.
- [60] K. Simonyan and A. Zisserman, “Very deep convolutional networks for large-scale image recognition,” *arXiv preprint arXiv:1409.1556*, 2014.
- [61] M. Tan and Q. V. Le, “Efficientnet: Rethinking model scaling for convolutional neural networks,” 2020.
- [62] K. He, X. Zhang, S. Ren, and J. Sun, “Deep residual learning for image recognition,” in *Proceedings of the IEEE conference on computer vision and pattern recognition*, pp. 770–778, 2016.
- [63] C. Szegedy, V. Vanhoucke, S. Ioffe, J. Shlens, and Z. Wojna, “Rethinking the inception architecture for computer vision,” in *Proceedings of the IEEE conference on computer vision and pattern recognition*, pp. 2818–2826, 2016.
- [64] W. Liao, X. Chen, X. Lu, Y. Huang, and Y. Tian, “Deep transfer learning and time-frequency characteristics-based identification method for structural seismic response. front,” *Built Environ*, vol. 7, no. 10, 2021.

- [65] G. Kim, B. Ku, and H. Ko, “Multifeature fusion-based earthquake event classification using transfer learning,” *IEEE Geoscience and Remote Sensing Letters*, vol. 18, no. 6, pp. 974–978, 2020.
- [66] A. Pignatelli, F. D’Ajello Caracciolo, and R. Console, “Automatic inspection and analysis of digital waveform images by means of convolutional neural networks,” *Journal of Seismology*, vol. 25, no. 6, pp. 1347–1359, 2021.
- [67] G. Mishne and I. Cohen, “Iterative diffusion-based anomaly detection,” in *2017 IEEE International Conference on Acoustics, Speech and Signal Processing (ICASSP)*, pp. 1682–1686, IEEE, 2017.
- [68] D. Dov, R. Talmon, and I. Cohen, “Audio-visual voice activity detection using diffusion maps,” *IEEE/ACM Transactions on Audio, Speech, and Language Processing*, vol. 23, no. 4, pp. 732–745, 2015.
- [69] N. Rabin, M. Kahlon, S. Malayev, and A. Ratnovsky, “Classification of human hand movements based on emg signals using nonlinear dimensionality reduction and data fusion techniques,” *Expert Systems with Applications*, vol. 149, p. 113281, 2020.
- [70] S. Alagapan, H. W. Shin, F. Fröhlich, and H.-t. Wu, “Diffusion geometry approach to efficiently remove electrical stimulation artifacts in intracranial electroencephalography,” *Journal of neural engineering*, vol. 16, no. 3, p. 036010, 2019.
- [71] S. Lafon, Y. Keller, and R. R. Coifman, “Data fusion and multicue data matching by diffusion maps,” *IEEE Transactions on pattern analysis and machine intelligence*, vol. 28, no. 11, pp. 1784–1797, 2006.
- [72] E. J. Nyström, *Über die praktische auflösung von linearen integralgleichungen mit anwendungen auf randwertaufgaben der potentialtheorie*. Akademische Buchhandlung, 1929.
- [73] L. Delves and J. Walsh, “Numerical solution of integral equations, clarendon,” 1974.

- [74] A. Bermanis, A. Averbuch, and R. R. Coifman, “Multiscale data sampling and function extension,” *Applied and Computational Harmonic Analysis*, vol. 34, no. 1, pp. 15–29, 2013.
- [75] N. Rabin and R. R. Coifman, “Heterogeneous datasets representation and learning using diffusion maps and laplacian pyramids,” in *Proceedings of the 2012 SIAM International Conference on Data Mining*, pp. 189–199, SIAM, 2012.
- [76] R. R. Coifman and S. Lafon, “Geometric harmonics: a novel tool for multiscale out-of-sample extension of empirical functions,” *Applied and Computational Harmonic Analysis*, vol. 21, no. 1, pp. 31–52, 2006.
- [77] C. J. Dsilva, R. Talmon, N. Rabin, R. R. Coifman, and I. G. Kevrekidis, “Non-linear intrinsic variables and state reconstruction in multiscale simulations,” *The Journal of chemical physics*, vol. 139, no. 18, p. 11B608\_1, 2013.
- [78] Á. Fernández, N. Rabin, R. R. Coifman, and J. Eckstein, “Diffusion methods for aligning medical datasets: location prediction in ct scan images,” *Medical image analysis*, vol. 18, no. 2, pp. 425–432, 2014.
- [79] R. Talmon, I. Cohen, and S. Gannot, “Supervised source localization using diffusion kernels,” in *2011 IEEE workshop on applications of signal processing to audio and acoustics (WASPAA)*, pp. 245–248, IEEE, 2011.
- [80] R. Talmon, D. Kushnir, R. R. Coifman, I. Cohen, and S. Gannot, “Parametrization of linear systems using diffusion kernels,” *IEEE Transactions on Signal Processing*, vol. 60, no. 3, pp. 1159–1173, 2011.
- [81] P. M. Shearer, *Introduction to seismology*. Cambridge university press, 2019.
- [82] J. Havskov and G. Alguacil, *Instrumentation in earthquake seismology*, vol. 358. Springer, 2004.
- [83] P. Bormann, “Seismic arrays,” in *New manual of seismological observatory practice* (J. Schweitzer, J. Fyen, and S. Mykkeltveit, eds.), ch. 9, pp. 1–80, Potsdam, Germany: GeoForschungsZentrum, 2012.

- [84] P. Bormann, “Data analysis and seismogram interpretation,” in *New Manual of Seismological Observatory Practice 2 (NMSOP-2)* (K. Klinge and S. Wendt, eds.), ch. 11, pp. 1–126, Deutsches GeoForschungsZentrum GFZ, 2014.
- [85] R. V. Allen, “Automatic earthquake recognition and timing from single traces,” *Bulletin of the seismological society of America*, vol. 68, no. 5, pp. 1521–1532, 1978.
- [86] R. Allen, “Automatic phase pickers: Their present use and future prospects,” *Bulletin of the Seismological Society of America*, vol. 72, no. 6B, pp. S225–S242, 1982.
- [87] P. Bormann, “Understanding and parameter setting of sta/lta trigger algorithm,” in *New Manual of Seismological Observatory Practice 2 (NMSOP-2)* (A. Trnkoczy, ed.), pp. 1–20, Deutsches GeoForschungsZentrum GFZ, 2012.
- [88] Y. B. Horin and D. M. Steinberg, “Scoring idc sel1 events for identifying misformed events,” *Journal of seismology*, vol. 17, no. 4, pp. 1109–1123, 2013.
- [89] J. P. M. Company, “Mining and mines, eshidiya mine (last accessed july 2021).”
- [90] Z. S. Abu-Hamatteh, “Geology, geochemistry and are characteristics of the jordanian phosphates,” *Central European Geology*, vol. 50, no. 3, pp. 283–295, 2007.
- [91] R. Hofstetter, Y. Gitterman, V. Pinsky, N. Kraeva, and L. Feldman, “Seismological observations of the northern dead sea basin earthquake on 11 february 2004 and its associated activity,” *Isr. J. Earth Sci*, vol. 57, pp. 101–124, 2008.
- [92] M. Joswig, “Pattern recognition for earthquake detection,” *Bulletin of the Seismological Society of America*, vol. 80, no. 1, pp. 170–186, 1990.
- [93] S. Lloyd, “Least squares quantization in pcm,” *IEEE transactions on information theory*, vol. 28, no. 2, pp. 129–137, 1982.
- [94] J. MacQueen *et al.*, “Some methods for classification and analysis of multivariate observations,” in *Proceedings of the fifth Berkeley symposium on*

*mathematical statistics and probability*, vol. 1, pp. 281–297, Oakland, CA, USA, 1967.

- [95] J. Yosinski, J. Clune, Y. Bengio, and H. Lipson, “How transferable are features in deep neural networks?,” *arXiv preprint arXiv:1411.1792*, 2014.
- [96] A. Paszke, S. Gross, F. Massa, A. Lerer, J. Bradbury, G. Chanan, T. Killeen, Z. Lin, N. Gimelshein, L. Antiga, *et al.*, “Pytorch: An imperative style, high-performance deep learning library,” *Advances in neural information processing systems*, vol. 32, pp. 8026–8037, 2019.
- [97] D. P. Kingma and J. Ba, “Adam: A method for stochastic optimization,” *arXiv preprint arXiv:1412.6980*, 2014.
- [98] A. J. Rodgers, T. Lay, W. R. Walter, and K. M. Mayeda, “A comparison of regional-phase amplitude ratio measurement techniques,” *Bulletin of the Seismological Society of America*, vol. 87, no. 6, pp. 1613–1621, 1997.

## תקציר

למידת יריעה הוא ענף של למידת מכונה המספק כלים רביעצמה לניתוח נתונים רב-מדדים מורכבים. שיטות אלו מתאימות במיוחד לפיתוח טכניקות חדשות ויעילות של עיבוד אוטומטי, שיכלולו לארגן את מערכיו הנთונים לפי הפרמטרים החבויים שלהם תוך שמירה על הגיאומטריה של המרחב הפיזי. לשם כך, הוצגה מודיפיקציה של מפות דיפוזיה, שהיא שיטת למידת יריעה על בסיס גיאומטרי. מודיפיקציה זו משלבת גרעינים אנאייזוטרופיים לתוך מערכת מפות הדיפוזיה. דוגמה לתהום מחקר שנייה למודל תוך שימוש בклים אלו היא הסיווג של מחלקה יעד ספציפית, הידועה גם בשם סיווג מחלקה-יחידה. הרעיון הוא לבנות מודל מבוסס למידת יריעה שמצד אחד יזהה את הדגימות השויות למחלקה היעד, ומצד שני יספק ארגון של הדגימות ממחלקה היעד על פי הפרמטרים החשובים של מחלקה זו.

בעבודה זו, אנו מציעים למודל בעית סיווג מחלקה-יחידה עם מפות דיפוזיה אנאייזוטרופיות, על בסיס מודל זה אנו בונים מודל מפות דיפוזיה מבוסס רפנס. כדי להציג את היתרונות של השיטה שלנו, פיתחנו אפליקציה חדשנית המאפשרת מילול של אירועים סיסמיים, של מחלקה יעד ספציפית, הקשורים בגיאומטריה אותן-מרחבי משותפת. אנו מבצעים זיהוי אוטומטי של פיצוצי מהצבה שמקומם במחצבה ספציפית, בהינתן זרם נתונים סיסמיים, בעלות חשיבות נמוכה. דפוס המצחבה לזיהוי הוא מורכב ומאתגר, מכיוון שהוא מכיל אירועים סיסמיים מגוונים ורעים. היכולות של האפליקציה מוצגות עבור מספר נתונים גדולים המתוארים על ידי מומחי מרcco הנתונים הלאומי של ישראל, והושוו עם טכניקות למידה عمוקה. יתר על כן, אנו משלבים טכניקות להיתוך נתונים ממספר חישנים והרחבת המודל לדגימות חדשות הנמדדות באופן שוטף. התוצאות שלנו מראות שלמעלה מ-99% מפיצוצי המצחבה החדשים סוגו בצהרה נכונה. השיטה המוצעת יכולה להתאים לסוגים אחרים של יישומי זיהוי תבניות, כגון זיהוי דיבור וראייה ממוחשבת.

## **אוניברסיטת תל אביב**

הפקולטה להנדסה ע"ש איבי ואלדר פליישמן  
בית הספר לתחומים מתקדמים ע"ש זנדמן סליינר

## **מפות דיפוזיה על בסיס רפנס עבור סיוג מחלקה-יחידה: אפליקציה לזיהוי פיצוצי מהצבה**

חיבור זה הוגש כעבודה גמר לקרהת התואר  
”מוסמך אוניברסיטה” בהנדסת חשמל  
על ידי

## **איתן ניב**

העבודה נעשתה בבית הספר להנדסת חשמל  
הפקולטה להנדסה  
בהנחיית ד"ר נתע רבין וד"ר יורי ברגמן

ניסן תשפ"ב

## **אוניברסיטת תל אביב**

הפקולטה להנדסה ע"ש איבי ואלדר פליישמן  
בית הספר לתחומים متقدמים ע"ש זנדמן סליינר

# **מפות דיפוזיה על בסיס רפנס עבור סיוג מחלקה-יחידה: אפליקציה לזיהוי פיצוצי מהצבה**

חיבור זה הוגש כעבודת גמר לקרأت התואר  
”מוסמך אוניברסיטה” בהנדסת חשמל

על ידי

## **איתן ניב**

ניסן תשפ"ב